

# The eROSITA Final Equatorial-Depth Survey (eFEDS): The Catalog of Galaxy Clusters and Groups

A. Liu<sup>1\*</sup>, E. Bulbul<sup>1</sup>, V. Ghirardini<sup>1</sup>, T. Liu<sup>1</sup>, M. Klein<sup>2</sup>, N. Clerc<sup>3</sup>, Y. Özsöy<sup>1</sup>, M. E. Ramos-Caja<sup>1</sup>, F. Pacaud<sup>4</sup>, J. Comparat<sup>1</sup>, N. Okabe<sup>5, 6, 7</sup>, Y. E. Bahar<sup>1</sup>, V. Biffi<sup>2, 8, 9</sup>, H. Brunner<sup>1</sup>, M. Brüggen<sup>10</sup>, J. Buchner<sup>1</sup>, J. Ider Chitham<sup>1</sup>, I. Chiu<sup>11, 12, 13</sup>, K. Dolag<sup>2</sup>, E. Gatuzz<sup>1</sup>, J. Gonzalez<sup>1</sup>, D. N. Hoang<sup>10</sup>, G. Lamer<sup>14</sup>, A. Merloni<sup>1</sup>, K. Nandra<sup>1</sup>, M. Oguri<sup>15, 16, 17</sup>, N. Ota<sup>4, 18</sup>, P. Predehl<sup>1</sup>, T. H. Reiprich<sup>4</sup>, M. Salvato<sup>1</sup>, T. Schrabback<sup>4</sup>, J. S. Sanders<sup>1</sup>, R. Seppi<sup>1</sup>, Q. Thibaud<sup>3</sup>

(Affiliations can be found after the references)

June 29, 2021

## ABSTRACT

**Aims.** The eROSITA Final Equatorial-Depth Survey has been carried out during the Performance Verification phase of the Spectrum-Roentgen-Gamma/eROSITA telescope and completed in November 2019. This survey is designed to provide the first eROSITA-selected sample of clusters and groups and to test the predictions for the all-sky survey in the context of cosmological studies with clusters of galaxies.

**Methods.** In the  $\sim 140$  square degree area covered by eFEDS, 542 candidate clusters and groups of galaxies are detected as extended X-ray sources with the eSASS source detection algorithm. In this work, we perform imaging and spectral analysis on the 542 cluster candidates with eROSITA X-ray data, and study the properties of the sample.

**Results.** We provide the catalog of candidate galaxy clusters and groups detected by eROSITA in the eFEDS field, down to a flux of  $\sim 10^{-14}$  erg s $^{-1}$  cm $^{-2}$  in the soft band (0.5–2 keV) within 1'. The clusters are distributed in the redshift range  $z = [0.01, 1.3]$ , with the median redshift  $z_{\text{median}} = 0.35$ . With eROSITA X-ray data, we measure the intracluster medium (ICM) temperature within two radii, 300 kpc and 500 kpc, and constrain the temperature with  $> 2\sigma$  confidence level for  $\sim 1/5$  (102/542) of the sample. The average temperature of these clusters is  $\sim 2$  keV. Radial profiles of flux, luminosity, electron density, and gas mass are measured from the precise modeling of the imaging data. The selection function, the purity and completeness of the catalog are examined and discussed in detail. The contamination fraction is  $\sim 1/5$  in this sample, dominated by misidentified point sources. The X-ray Luminosity Function (XLF) of the clusters agrees well with the results obtained from other recent X-ray surveys. We also find 19 supercluster candidates in this field, most of which are located at redshifts between 0.1 and 0.5, including the one at  $z \sim 0.36$ , which is already presented in Ghirardini et al. (2021).

**Conclusions.** The eFEDS cluster and group catalog at the final eRASS equatorial depth provides a benchmark proof-of-concept for the eROSITA All-Sky Survey extended source detection and characterization. We confirm the excellent performance of eROSITA for cluster science and expect no significant deviations from our pre-launch expectations for the final All-Sky Survey.

**Key words.** surveys – galaxies: clusters: general – galaxies: clusters: intracluster medium – X-rays: galaxies: clusters

## 1. Introduction

The extended ROentgen Survey with an Imaging Telescope Array (eROSITA, Predehl et al. 2021) onboard the Spectrum-Roentgen-Gamma (SRG) mission is a German-Russian X-ray telescope launched on July 13, 2019. With the large collecting area (1365 cm $^2$  at 1 keV), moderate angular resolution (on-axis half energy width HEW  $\sim 18''$  at 1.49 keV), and wide energy band coverage (0.2–10 keV) (Predehl et al. 2021), eROSITA will provide an X-ray all-sky survey with unprecedented sensitivity. The complete eROSITA All-Sky Survey (eRASS) will be about 25 times more sensitive than the ROSAT All-Sky Survey (RASS, Voges et al. 1999) in the soft X-ray band (0.2–2.3 keV), and will be the first ever true X-ray imaging all-sky survey in the hard band (2.3–10 keV) (Merloni et al. 2012). The final eROSITA All-Sky Survey will consist of eight complete scans of the X-ray sky by the end of 2023, each lasting for six months. The first and second scans have already been completed in June and December, 2020.

One of the main science goals of eROSITA is to study cosmology by detecting a large number of galaxy clusters and

groups<sup>1</sup> which are the main extended sources in the X-ray sky. Clusters are the most massive gravitationally bound systems in the Universe. Located at the crossroads between cosmology and astrophysics, clusters play an irreplaceable role to trace the formation and evolution of the large-scale structure (see Allen et al. 2011, for a review), as well as the various astrophysical processes on smaller scales (e.g., Rosati et al. 2002). Studies on cluster-related cosmology and astrophysics both require a large sample of clusters with a clean selection function and an accurate mass calibration (see, e.g. Pratt et al. 2019).

The first X-ray imaging all-sky survey, RASS, was performed by ROSAT in 1990s (Voges et al. 1999), which surveyed the X-ray sky in the soft (0.1–2.4 keV) band. RASS-based catalogs, such as BCS (ROSAT Brightest Cluster Sample, Ebeling et al. 1998), NORAS (Northern ROSAT All-Sky Galaxy Cluster Survey, Böhringer et al. 2000), REFLEX (ROSAT-ESO Flux Limited X-ray Galaxy Cluster Survey, Böhringer et al. 2001), MACS (Massive Cluster Survey, Ebeling et al. 2001), CIZA (Clusters In the Zone of Avoidance, Ebeling et al. 2002), and sev-

<sup>1</sup> For simplicity, in this paper we will use “clusters” to refer to the assembly of X-ray emitting galaxy clusters and groups, unless noted otherwise.

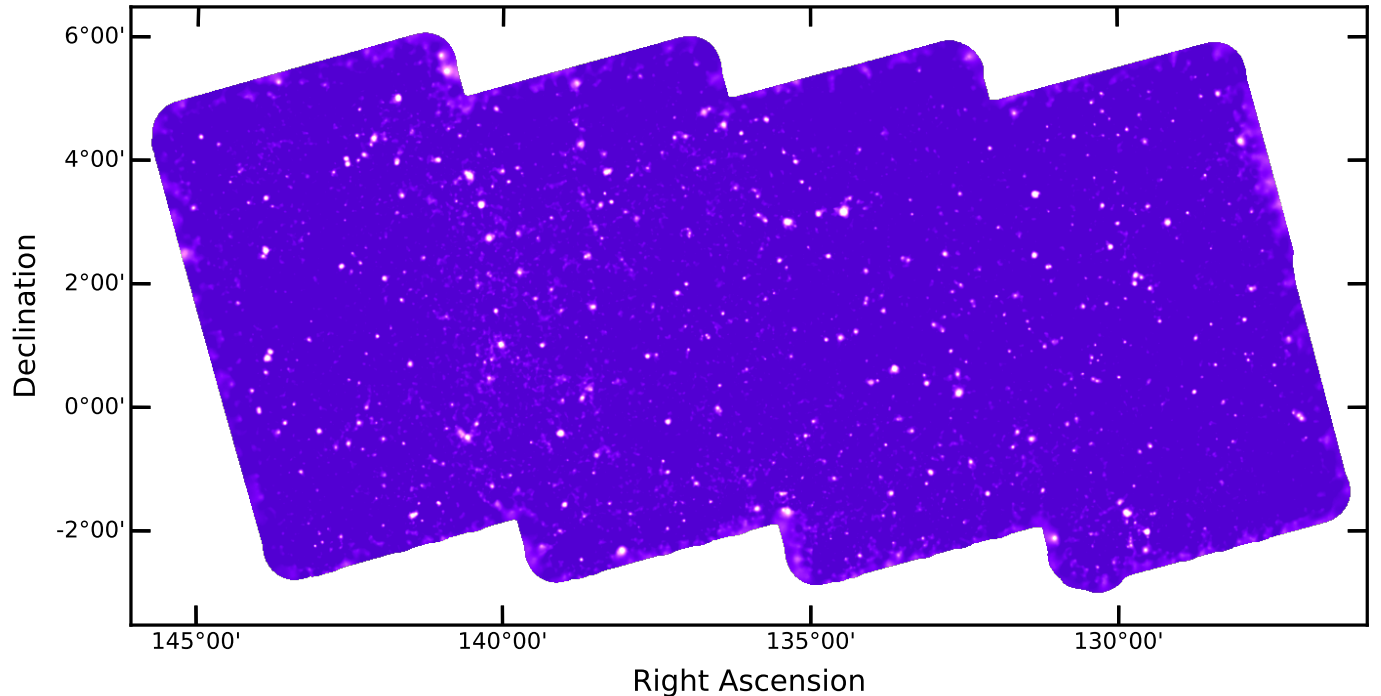


**Fig. 1.** Exposure-corrected point-source free 0.2–2.3 keV adaptively-smoothed eROSITA image of the eFEDS field. In detail, a point source mask is constructed by excluding regions around each point source where the surface brightness is above 10% of the background surface brightness. The `accumulate_counts` program from the Contour Binning package (Sanders & Fabian 2006) is used to calculate a map containing the radius around each pixel (including those in masked areas) which encloses at least 36 counts (excluding masked sources). This map is used to smooth the input image and exposure map by Gaussians, excluding masked areas, where  $\sigma$  is given by the radius in each pixel. The smoothed image and exposure map are divided to make the exposure-corrected image shown here.

eral other catalogs compiled in more recent years (see, e.g., Piffaretti et al. 2011; Böhringer et al. 2014, 2017; Klein et al. 2019; Finoguenov et al. 2020), contain a few thousand clusters in total, reaching a flux limit of  $\sim 10^{-12}$  erg s $^{-1}$  cm $^{-2}$ . However, the sensitivity of ROSAT limits its capability to detect high-redshift and low-mass clusters. In the last ten years, the Sunyaev-Zeldovich (SZ) effect surveys, such as SPT (South Pole Telescope, Bleem et al. 2015), ACT (Atacama Cosmology Telescope, Hasselfield et al. 2013), and *Planck* (*Planck Collab.* et al. 2014), have also made a remarkable contribution to the increase in ICM-based cluster sample. Nevertheless, the thermodynamical and chemical properties of the SZ selected clusters also need to be measured from X-ray follow-up observations. Moreover, X-ray surveys are more sensitive in detecting low-mass nearby clusters compared to other bands such as SZ and optical, and are less affected by projection effects. It is therefore necessary to establish a larger and deeper X-ray cluster sample, which effectively extends to high-redshift and low-mass regimes.

In the years after RASS, a number of small- and medium-area X-ray surveys have been conducted based on *XMM-Newton* and *Chandra* (see, e.g., Hasinger et al. 2007; Cappelluti et al. 2007; Finoguenov et al. 2007; Pierre et al. 2007; Finoguenov et al. 2010; Clerc et al. 2012; Finoguenov et al. 2015; Pierre et al. 2016; Gozaliasl et al. 2019; Koulouridis et al. 2021). Despite that the sky coverage of most of these surveys is smaller than 100 square degrees, hundreds of clusters have been detected, reaching fluxes of  $10^{-15}$  erg s $^{-1}$  cm $^{-2}$ , thanks to the high sensitivity of the instruments and the sufficient depth of the surveys. With well-understood selection functions and extensive follow-up observations, these samples play an important

role in the study of cluster physics and the constraints of cosmology (see, e.g., Pacaud et al. 2016; Ridl et al. 2017; Adami et al. 2018; Pacaud et al. 2018), filling the gap between RASS and the next generation of X-ray all-sky survey. As the successor of ROSAT, one of the main design goals of eROSITA is to provide a larger X-ray selected sample of clusters. eROSITA is expected to detect  $\sim 10^5$  clusters in the complete all-sky survey (Merloni et al. 2012; Pillepich et al. 2012), up to redshifts  $z \sim 1.5$ , down to masses of  $M_{500} \sim 10^{13} M_\odot$ , and reaching a flux limit of  $f_{0.5-2 \text{ keV}} \sim 10^{-14}$  erg s $^{-1}$  cm $^{-2}$ . This cluster catalog will inevitably be a valuable resource to test and constrain cosmological models, to trace the evolution of the large-scale structure, and to study cluster-related astrophysics.

A proof-of-concept mini-survey, the eROSITA Final Equatorial-Depth Survey (eFEDS), was designed to demonstrate the survey science capabilities of eROSITA. The observations of the eFEDS field were performed between November 4th to 7th, 2019, during the Performance Verification (PV) phase. The eFEDS field is located at  $126^\circ < \text{R.A.} < 146^\circ$  and  $-3^\circ < \text{Dec.} < +6^\circ$ , covering a solid angle of approximately 140 square degrees<sup>2</sup>, with the similar depth as the full eROSITA All-Sky Survey in the equatorial regions. The average exposure times are  $\sim 2.2$  ks and  $\sim 1.2$  ks, before and after correcting for vignetting effects. The eFEDS field has also been observed with a broad array of multi-wavelength survey instruments, from optical to radio bands. In particular, the photometric data from the Hyper Suprime-Cam (HSC) Subaru Strategic Program (HSC-SSP; Ai-hara et al. 2018b,a; Miyazaki et al. 2018; Komiyama et al. 2018;

<sup>2</sup> 137.9 deg $^2$  have a vignetting-corrected exposure time in the 0.5–2 keV band of 0.1 ks or more.

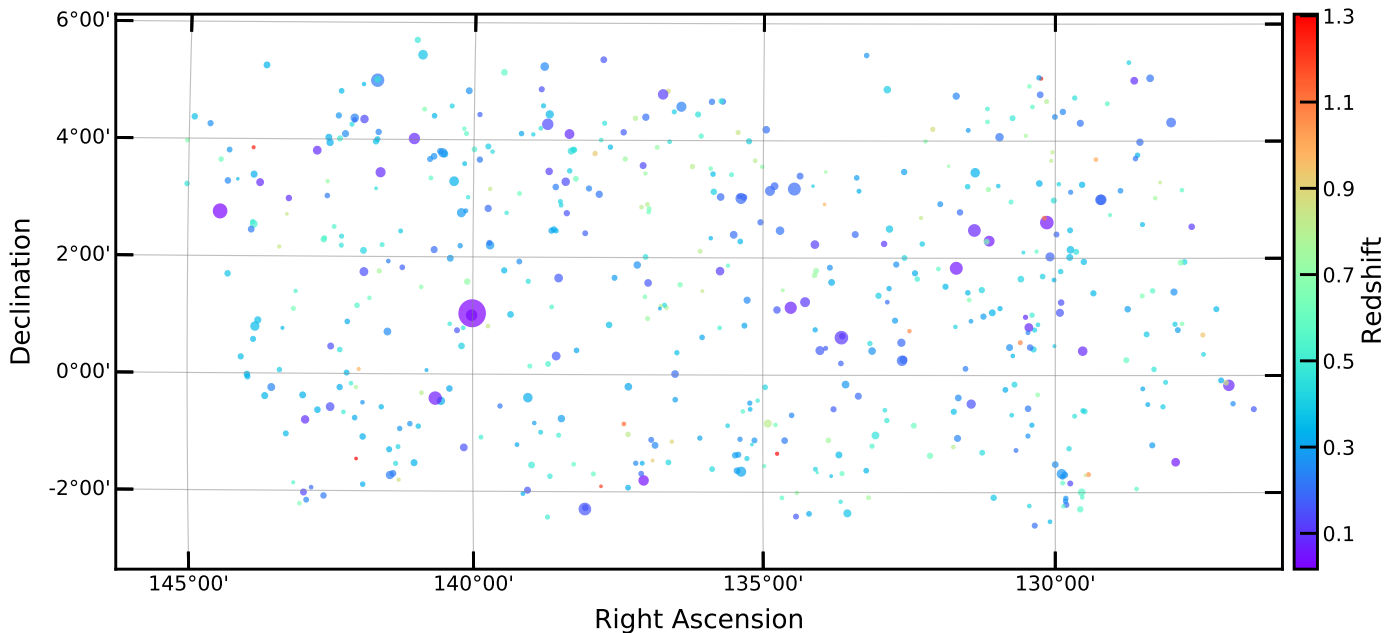


**Fig. 2.** Distribution of the 542 cluster candidates in eFEDS. Color code represents the redshift of the cluster, provided by MCMF (Multi-Component Matched Filter, Klein et al. 2018, 2019). The radius of the circle is equal to  $R_{500}$ , within which the average density is 500 times the critical density at the cluster's redshift.

Kawanomoto et al. 2018; Furusawa et al. 2018; Bosch et al. 2018; Huang et al. 2018; Coupon et al. 2018; Oguri et al. 2018; Aihara et al. 2019), DECaLS (Dark Energy Camera Legacy Survey, Dey et al. 2019), SDSS (Sloan Digital Sky Survey, Blanton et al. 2017), 2MRS (2MASS Redshift Survey, Huchra et al. 2012), and GAMA (Galaxy And Mass Assembly, Driver et al. 2009) surveys are used for cluster optical confirmation and redshift determination, and HSC, in particular, will provide weak lensing masses for eFEDS clusters (Klein et al., accepted, Chiu et al., submitted). Combining these with the X-ray properties measured with eROSITA data will enable the calibration of scaling relations between X-ray observables and cluster halo mass (Bahar et al., in prep, Ghirardini et al., submitted). Being the largest contiguous survey at the final Equatorial depth, it provides an ideal set-up for testing the predictions for the cluster number density in the survey and offers rich cluster science through its multi-wavelength coverage (e.g., Ghirardini et al. 2021, Pasini et al., submitted).

In this paper, we present the catalog of candidate galaxy clusters and groups detected in eFEDS, and provide the first results of the X-ray analysis on these clusters based on eROSITA data. More in-depth studies about the eFEDS clusters will also be presented in a series of accompanying and forthcoming papers. In Klein et al. (accepted), we present the optical identification of the eFEDS cluster candidates. In Chiu et al. (submitted), Ramos et al. (in prep.), and Ota et al. (in prep.), we perform optical and weak lensing analysis on the eFEDS clusters. Radio properties of the clusters are studied in Pasini et al. (submitted). ICM morphology and X-ray scaling relations based on eROSITA data are studied in Ghirardini et al. (submitted) and Bahar et al. (in prep.), respectively. Spectroscopic follow-up results will be provided in Ider Chitham et al. (in prep.). The catalog of cluster candidates misidentified as point sources will be presented in Bulbul et al. (in prep.). Moreover, the main eFEDS X-ray source catalog is provided in Brunner et al. (submitted). The eFEDS simulation results are introduced in detail in Liu et al. (submitted).

The paper is organized as follows. In Sect. 2, we describe in detail the eROSITA observations on the eFEDS field and the source detection, and discuss the potential contamination in the sample. We also summarize in this section the optical confirmation and redshift determination of the clusters on basis of optical photometric and spectroscopic survey data. In Sect. 3, we examine the selection function of the cluster sample. In Sect. 4, we provide the details of the X-ray data analysis we performed in this work as well as X-ray observables. In Sect. 5, we compute the X-ray luminosity function of the cluster sample. In Sect. 6, we perform a search for superclusters in the eFEDS field, on basis of the spatial distribution and redshifts of the clusters. Our conclusions are summarized in Sect. 7. Throughout this paper, we adopt the concordance  $\Lambda$ CDM cosmology with  $\Omega_\Lambda = 0.7$ ,  $\Omega_m = 0.3$ , and  $H_0 = 70 \text{ km s}^{-1} \text{ Mpc}^{-1}$ . Quoted error bars correspond to a  $1-\sigma$  confidence level, unless noted otherwise.

## 2. eFEDS Extended Source Catalog

### 2.1. eROSITA Observation and Data Calibration

The data are processed with the eROSITA Standard Analysis Software System (eSASS, Brunner et al., submitted)<sup>3</sup>. The details of the data reduction and calibration are described in Brunner et al., (submitted) and Dennerl et al. (2020), we here provide a short summary of the analysis steps. Pattern recognition and energy calibration are applied for all the seven eROSITA telescope modules (TMs) to produce calibrated event lists. The event lists are then filtered after the determination of good time intervals, dead times, corrupted events and frames, and bad pixels. Using star-tracker and gyro data, celestial coordinates are assigned to the reconstructed X-ray photons, which can then be projected on the sky so images and exposure maps can be produced. In this work, we select all valid pixel patterns, i.e., single, double, triple,

<sup>3</sup> version eSASSusers\_201009.

and quadruple events, but use only photons which are detected at off-axis angles  $\leq 30'$ . By doing this, we remove the photons in the corners of the square CCDs where the vignetting and point spread function (PSF) calibrations are currently less accurate.

## 2.2. Source Detection Strategy

The details about source detection for eFEDS are presented in Brunner et al., (submitted). Here we will briefly summarize the compilation of the extended source catalog. The source detection was performed using the tool `erbox` in eSASS, on the merged 0.2–2.3 keV image of all seven eROSITA TMs. `erbox` is a modified sliding box algorithm, which searches for sources on the input image that are brighter than the expected background fluctuation at a given image position. The source detection procedure contains the following steps. As the first step, `erbox` is applied to scan the X-ray image with a local sliding window, and returns a list of candidate sources, which are enhancements with respect to the background above a certain threshold. The background is interpolated from a frame-shaped region around the detection window. The candidate sources identified in the first step are then excised from the original image. The resulting source-free image is then used to create a background map via adaptive filtering using the `erbackmap` tool in eSASS. The source detection with `erbox` is then repeated, but using the new background map created in the last step, producing a new list of candidate sources. The `erbox+erbackmap` iteration is run three times, to enhance the reliability of the background map, and the sensitivity of the detection algorithm.

In the second step, the source parameters for each candidate, such as the detection likelihood, the extent likelihood, and the extent, are determined by fitting the image with the source model, which is a  $\beta$ -model convolved with the calibrated PSF, in which  $r_c$  equals to the extent of the source, and is set free to vary between 8'' and 60'' for extended sources. This step is performed using the `ermldet` tool in eSASS.

We apply the above source detection procedures on the 0.2–2.3 keV image of the eFEDS field. Setting the minimum detection likelihood,  $\mathcal{L}_{\text{det}} \equiv -\ln(P)$ , at 5, and the minimum extent likelihood  $\mathcal{L}_{\text{ext}}$  at 6, we detect 542 candidate extended sources over the full eFEDS field. This corresponds to an extended source density of  $\sim 4$  per square degree at the Equatorial depth. The eROSITA image of the eFEDS field with the extended sources being highlighted is shown in Fig. 1. The distribution of the sources in the field with redshift information (see Section 2.3) is shown in Fig. 2.

## 2.3. Optical Confirmation and Redshift Determination

The determination of photometric redshifts of the clusters are based on the Multi-Component Matched Filter (MCMF) cluster confirmation tool (see Klein et al. 2018, 2019, for more details). The MCMF tool takes optical photometric datasets, and searches for galaxy overdensities along the line of sight at the position of a cluster candidate. For that, the galaxy cluster richness is measured as a function of redshift using a red-sequence technique and within an aperture defined from the X-ray count rate. Peaks in richness versus redshift space are fitted by specific peak profiles and redshift and richnesses are recorded for multiple possible counterparts along the line of sight. MCMF is then run on random lines of sight excluding regions around X-ray candidates. MCMF on eFEDS was run on two photometric datasets with different optical filters and depth: DECaLS  $g, r, z$

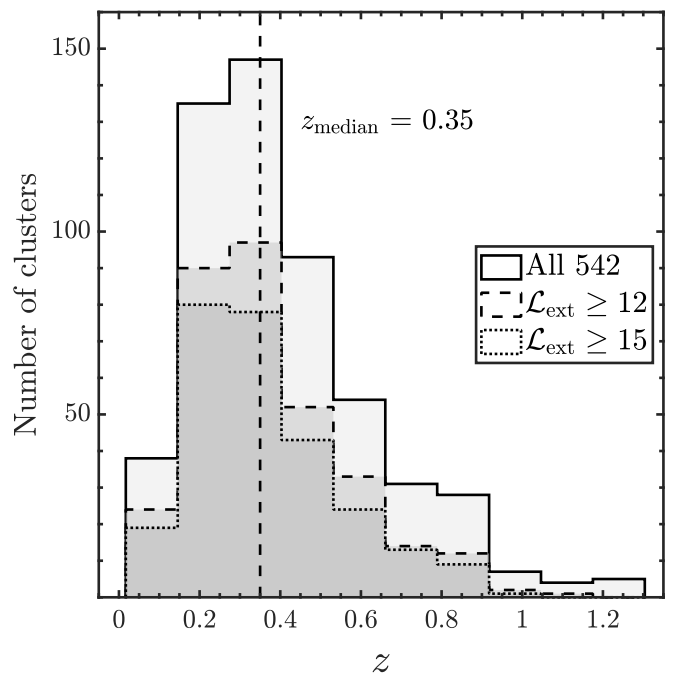


**Fig. 3.** Redshift histogram of the 542 cluster candidates in the redshift range of 0.01 to 1.3. The median redshift of the sample  $z_{\text{median}}=0.35$  is shown as the vertical dashed line. Also plotted are the results after cutting the sample with different thresholds on the extent likelihood  $\mathcal{L}_{\text{ext}}$ .

and unWISE W1 bands, and HSC  $g, r, i, z$  bands. DECaLS does not suffer from strong calibration issues, and provides full coverage of the eFEDS field, but is  $\sim 2$  magnitudes shallower than HSC-SSP data. The deep HSC-SSP data in the  $g, r, i, z$  bands provide good photometric redshifts out to high redshifts ( $z \sim 1.3$ ), where DECaLS suffers from shallower data and missing  $i$ -band. The results of both MCMF runs were then combined to the final catalog. Spectroscopic redshifts, on the other hand, are then derived by cross matching the clusters with public spectroscopic redshifts including SDSS up to DR16 (Blanton et al. 2017), GAMA (Driver et al. 2009) and 2MRS (Huchra et al. 2012) and requiring either three or more redshifts consistent with the photo- $z$  estimate and within  $R_{500}$  (estimated using the relation between X-ray count rate and mass, see Klein et al., accepted), or a spectroscopic redshift of the brightest cluster galaxy (BCG). We note that the searching radius of  $R_{500}$  is large enough, as it is well beyond the typical offsets between the X-ray and optical center, or the BCG, of galaxy clusters (e.g., Seppi et al. 2020). In total, we provide spectroscopic redshifts for 296 clusters.

In Fig. 3, we plot the histogram of the 542 redshifts. The redshift of the clusters in the sample ranges from 0.01 to 1.3, with the median value  $z_{\text{median}} = 0.35$ . The distribution of redshift is very close to the prediction of Pillepich et al. (2012) when assuming a mass cut at  $M_{500} = 5 \times 10^{13} M_{\odot}$  (see their Fig. 3).

In our companion paper on the optical confirmation and redshifts (Klein et al., accepted), we provide a detailed description of the follow-up and analysis of its results. We refer the interested reader to the aforementioned paper for more details.

**Table 1.** Results of cross matching with published cluster catalogs.

Catalog	Survey type	Ref.	$d_{\text{match}}$	$N_{\text{match}}$
MCXC	X-ray	(1)	2'	1
CODEX	X-ray	(2)	2'	43
PLANCKSZ2	SZ	(3)	3'	10
ACT	SZ	(4)	2'	57

**Notes.** References: (1) Piffaretti et al. (2011), (2) Finoguenov et al. (2020), (3) Planck Collaboration et al. (2016a), (4) Hilton et al. (2021).

#### 2.4. Cross match with published X-ray and SZ cluster catalogs

The eFEDS field is also covered by other X-ray and SZ surveys. We therefore match our catalog to the published cluster catalogs. For X-ray clusters, we use the MCXC (Meta-Catalogue of X-ray detected Clusters of galaxies, Piffaretti et al. 2011) and the CODEX (COnstrain Dark Energy with X-ray clusters, Finoguenov et al. 2020), both of which are mainly based on the ROSAT all sky survey (MCXC also contains clusters from ROSAT pointed observations and *XMM-Newton* observations). For SZ clusters, we use the most recent ACT-DR5 cluster catalog (Hilton et al. 2021) and the PLANCKSZ2 catalog (Planck Collaboration et al. 2016a). The matching distance is determined as 2' for X-ray catalogs and ACT catalog, and 3' for PLANCKSZ2 catalog. We do not present here the cross match results with optical cluster catalogs, because of the quite different selection of clusters in optical surveys with respect to ICM-based surveys (see, e.g., Wen et al. 2012; Rykoff et al. 2016). The results of the match are listed in Table 1. In summary, we find 1 and 43 matches with the MCXC and CODEX catalogs, and 10 and 57 matches with the PLANCKSZ2 and ACT catalogs, including also multiple-to-one matches. After removing the cases which are matched in multiple catalogs, we find 86 matches in total between the 542 eFEDS clusters and these published catalogs, corresponding to  $\sim 16\%$  of the whole sample, thus indicating that the majority of the clusters are detected for the first time in ICM-based surveys. The redshift comparisons of the common clusters are given in Klein et al., (accepted).

Here we briefly compare the luminosity ( $L_{500}$  in 0.1–2.4 keV band) provided in the CODEX catalog and measured in this work (see Sect. 4 for the measurement of luminosity) for the common clusters. Among the 43 common clusters, we find 13 clusters with luminosity difference larger than  $2\sigma$ . In fact, CODEX measured higher luminosity than our results for all these 13 clusters. Clearly, this disagreement can be due to many possible reasons. First, the redshifts are different: in 4 out of the 13 clusters, the redshifts we adopt in this work is different by  $> 15\%$  than those used in the CODEX catalog. Second, both the centers of the clusters and the radii to measure luminosity differ a lot in the two catalogs: the offsets in the center of the 13 clusters range from  $\sim 30''$  to 2'. Given the better angular resolution of eROSITA with respect to ROSAT, the luminosity measured with ROSAT for these 13 clusters can possibly be biased by unresolved Active Galactic Nuclei (AGN). However, we do not make further comparison between the measurements of X-ray observables in the two catalogs, as it would require to revisit the details in the analysis of the CODEX clusters, which is beyond the goal of this paper.

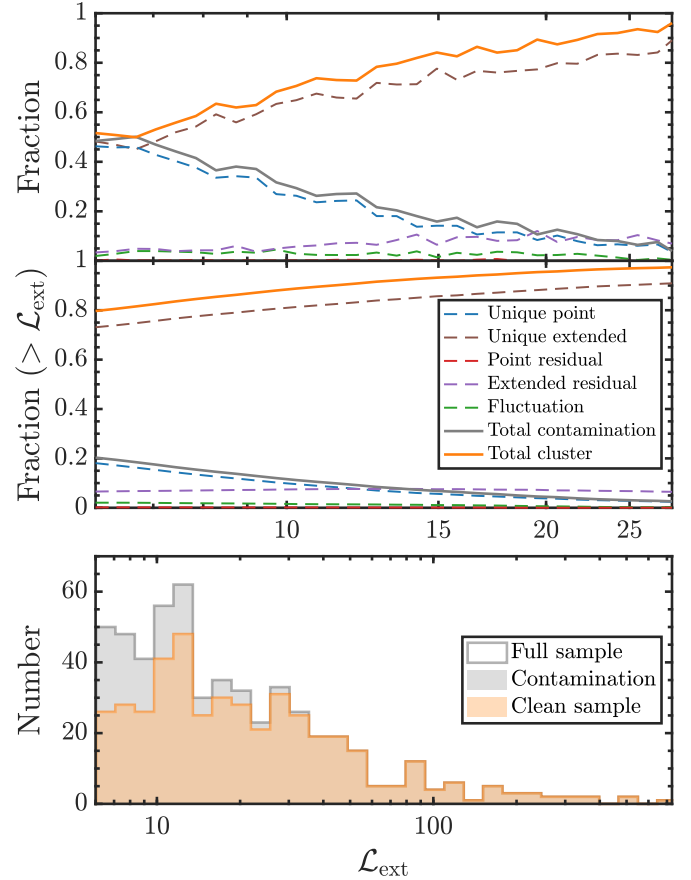


**Fig. 4.** Contamination fraction assessment in our sample based on simulations. *Upper panel:* The cumulative detection fraction of sources in the five classes as a function of extent likelihood. The orange solid line shows the total fraction of sources classified as real clusters, namely, the sum of unique extended source and extended source residual. Plotted as the gray solid line is the total contamination by summing up all the other three classes. *Middle panel:* The cumulative detecting fraction of sources in the five classes. *Lower panel:* the distribution of extent likelihood of the clusters in our catalog. Shown in orange color is the clean sample after removing the fraction of contamination. The gray bar represents the contamination in each bin.

#### 2.5. Contamination in the catalog

We use a set of realistic simulations of the eFEDS field using `sixte-2.6.2`<sup>4</sup> (Dauser et al. 2019) and `simput-2.4.10` to assess the contamination fraction in our catalog. The details of these simulations and their results are provided in Liu et al. (submitted) and Brunner et al. (submitted). The source detection and matching are performed on the simulated field in the same way as described in detail in Sect. 2.2. Here we use the simulations to estimate the total contamination in the catalog.

We divide the detected sources into the following five classes.

1. Unique point source, which is classified as a counterpart of an input AGN or a star.
2. Unique extended source, which is classified as a counterpart of an input extended source.

<sup>4</sup> <https://www.sternwarte.uni-erlangen.de/research/sixte/>

3. Point source residual. In this case, the input point source associated with the detected source has already been detected as a point source or an extended source. However, a part of its signal, likely in the outer wing of the PSF that cannot be perfectly fitted by the source detection algorithm, is detected as another point source.
4. Extended source residual. Similar to class 3, but the input source is an extended source. The input extended source has already been detected, but a part of its photons, which probably represent the signal from substructures or fluctuations in its outskirts, are detected as another extended source.
5. Background fluctuation, which is a source with no input counterpart, and classified as a spurious source due to background fluctuation.

We plot the detection fraction of the sources in each class as a function of the extent likelihood in Fig. 4. A cut at  $\mathcal{L}_{\text{ext}} > 6$  is applied to be consistent with our catalog. In Fig. 4, we consider classes 1, 3, and 5, the unique point source, point source residual, and background fluctuation, as contamination sources (i.e., non-cluster sources) in the catalog. Classes 2 and 4, the unique extended source and extended source residual, are classified as real clusters. In particular, we remark that we consider class 4 as real extended source instead of spurious detection, because substructures in cluster outskirts are commonly observed and it is reasonable to identify them as separated sources. The total fractions of contamination sources and clusters are also plotted in Fig. 4 as solid lines. From the top panel of Fig. 4, we can see that the contamination fraction can reach  $\sim 50\%$  at  $\mathcal{L}_{\text{ext}} = 6$ , and decreases to  $< 20\%$  at  $\mathcal{L}_{\text{ext}} = 15$ . We also found that, the contamination in the catalog is dominated by class 1, namely, the unique point sources, which are mostly AGN that are misidentified as extended sources. This is consistent with our previous simulation results (see Clerc et al. 2018, Fig. 9) which show that sources with low extent and low extent likelihood have higher probability to be point sources that are misidentified as extended. Combining the result with the distribution of  $\mathcal{L}_{\text{ext}}$  of our sample (see the middle and lower panels of Fig. 4), we find that, the total contamination fraction in our sample is  $\sim 1/5$ , corresponding to a total number of  $\sim 110$  non-cluster sources. Since most of these non-cluster sources have low  $\mathcal{L}_{\text{ext}}$ , they can be excluded by setting a  $\mathcal{L}_{\text{ext}}$  threshold much higher than 6. For example, a simple cut at  $\mathcal{L}_{\text{ext}} > 15$  delivers a subsample of  $\sim 270$  clusters with a purity  $> 90\%$ , despite that the sample volume is unavoidably reduced. We list in Table 2 the properties of the subsamples corresponding to different thresholds of  $\mathcal{L}_{\text{ext}}$ . The redshift distributions of the subsamples are plotted in Fig. 3. We remark that with the current eFEDS X-ray data alone, we are not able to perfectly clean the sample without significantly decreasing the sample volume. Deeper X-ray observations and multi-wavelength follow-ups are needed for further cleaning of the sample. For example, in Klein et al. (accepted), we present an approach to clean the sample making use of the optical information, which is found to remove a significant part of the contaminants. We refer the readers to the aforementioned paper for more details about the results and discussion on the optical cleaning of the sample.

We stress that our selection function is built based on the simulations of the X-ray sky coupled with the standard extended source detection procedure. Currently, the selection function does not include any information about the aforementioned optical cleaning. The modeling of the total selection function including both X-ray and optical information and cross-talk between these is being developed and subject to future work (Clerc et al. in prep.). To be consistent with our selection function, we

will include all the 542 cluster candidates in our further analysis in this paper, unless noted otherwise. We recommend the reader to use the X-ray extent and detection likelihood selections where the provided selection function is used for sample studies.

### 3. Selection Function

This section describes how the cluster sample completeness is inferred and the parameters it depends on. Simulations of the eFEDS field accounting for the instrument response function and the scanning strategy are described in Liu et al., (submitted). It relies on realistic methods to mock the emission of clusters of galaxies and AGN (Comparat et al. 2019, 2020).

#### 3.1. eFEDS field simulations

We recall here the main steps towards producing them. 18 independent realizations of the field are simulated in order to increase the statistics in the selection function derivation. A full sky light cone of dark matter halos is created based on the numerical N-body simulation (UNIT 1 inverse, Chuang et al. 2019), which assumes Planck-CMB cosmology (Planck Collaboration et al. 2016b). The halos are associated to X-ray emitting sources, namely AGN and galaxy clusters. The model of the X-ray emitting black hole population is empirical and inherits from the halo abundance matching technique that is particularly efficient at reproducing the observed stellar mass, luminosity and specific accretion rates distributions (Comparat et al. 2019). AGN fluxes are derived from a set of template spectra folded with a redshift- and luminosity-dependent obscuration model. For halos and subhalos with masses  $M_{500c}$  above  $5 \times 10^{13} M_{\odot}$ , cluster images are drawn from a library of emission measure profiles inferred from actual datasets, leading to reproducing the observed scaling relations between mass, luminosity and temperature (Comparat et al. 2020). The assignment between halos and profiles depends on their mass, redshift and dynamical state; a large positional offset between the dark matter center of mass and its highest density peak will preferentially lead to small central value of the emission measure profile. An ellipsoidal shape is given to cluster images that follows the halo triaxial shape. Halos of lower masses are simulated with the same method with the difference that we decrease their flux to obtain realistic fluxes for groups. Indeed the method suffers from the existing Malmquist bias in the library of profiles used and creates groups that are too bright. The source spectra are absorbed by an amount depending on the local Galactic absorption column density. Stellar sources as well as cosmic X-ray background and emission from the Galaxy are accounted for using measurements acquired during the Calibration and Performance Verification phases. The SIXTE simulation software (Dauver et al. 2019) is fed with the actual space-craft attitude file during the eFEDS mapping, hence the simulations faithfully reproduce the exposure variations in the field. Resulting event lists are processed similarly as the true eFEDS event lists, see Sect. 2.1. In particular, extended sources are identified by using identical thresholds in detection and extent likelihood as in the real catalog.

#### 3.2. Source counterpart finding

The matching between the input galaxy cluster catalogs and the extended source lists poses a challenge due to the richer sky density of the former as compared to the latter. Fixing a matching radius or performing a nearest neighbor search might lead to un-

**Table 2.** Properties of the subsamples corresponding to different thresholds of  $\mathcal{L}_{\text{ext}}$ .

Selection	Number of clusters	$z_{\text{median}}$	Flux limit (0.5–2 keV, 1 arcmin)	Completeness	Purity
Full sample	542	0.35	$10^{-14} \text{ erg s}^{-1} \text{ cm}^{-2}$	40%	80%
$\mathcal{L}_{\text{ext}} \geq 12$	325	0.34	$1.7 \times 10^{-14} \text{ erg s}^{-1} \text{ cm}^{-2}$	44%	>85%
$\mathcal{L}_{\text{ext}} \geq 15$	267	0.33	$2 \times 10^{-14} \text{ erg s}^{-1} \text{ cm}^{-2}$	47%	>90%

**Notes.** The completeness corresponds to the flux limit for each subsample. Purity is estimated from the simulation results in Liu et al. (submitted).

realistic matches because of projection effects. In order to mitigate this issue, we apply a Bayesian matching procedure that rests on the NWAY software and formalism (Salvato et al. 2018). Cross-correlation between both catalogs avoids specification of an explicit scale-length, except for a maximal radial search of 3' around each source, set to save computational cost. We account for angular extents by artificially increasing positional uncertainties of both input and detected sources. These uncertainties are set to 10% of a cluster virial radius, and to the best-fit source extent respectively. The NWAY algorithm is run twice, according to whether the input cluster list or the detection list is considered as the parent catalog. During both independent runs, a probability value  $p_i$  for an association to be valid is assigned to each pair composed of an input cluster and a detected source. An additional value  $p_{\text{any}}$  representing the probability for a source from the parent catalog to have at least one counterpart in the other catalog is also issued. These probabilities account for chance associations and provide a ranking of the most likely counterparts. Their values depend on the position of the sources, their positional uncertainties, the solid angle of the survey field, and the source density in both catalogs. In order to disentangle complex cases involving multiple substructures, heavy projection effects or substantial source splitting by the detection algorithms, we introduce a prior on the true flux distribution of detected sources. This prior updates the values of  $p_i$  and  $p_{\text{any}}$ . It is obtained by multiplying a loose version of the selection functions presented in Clerc et al. (2018) by the input flux distribution. By applying such prior, NWAY favors brighter sources when looking for counterparts to a detected source in the input cluster catalog. Finally, thresholds on  $p_{\text{any}}$  and  $p_i$  (two sets of thresholds for both runs) enable selection of valid matches. The final list of matches is found to be rather insensitive to the exact value of these thresholds: many of the  $p_{\text{any}}$  values are distributed either around zero or around one, and choosing  $p_i > 0.1$  proved to be efficient in selecting the correct counterpart. Valid matches with the highest  $p_i$  among all possible associations are denoted as primary matches; those matches that are primary in both runs are considered as solid matches between the input and detection lists.

### 3.3. Training classifiers

The main outcome of the matching procedure is a list of simulated clusters with associated properties and a flag indicating whether it is reliably matched to a detection. These properties are either intrinsic to a cluster (e.g., luminosity, redshift, central emission measure) or extrinsic (e.g., local exposure time, absorbing column density). We reformulate the problem of cluster selection into a binary classification problem and explored two methods to predict the detection probability of a cluster as a function of its properties.

The first set of selection functions relies on a random forest algorithm (e.g., Breiman 2001). We use the implementa-

tion present in the scikit-learn package<sup>5</sup> (Pedregosa et al. 2011). Properties attached to clusters, or features, are normalized and their one-dimensional distribution is rendered as flat as possible through histogram equalization. A balanced subsample from the initial list is created by randomly selecting 50% of the detected clusters and as many undetected objects. The remaining sources are kept for testing and evaluation purposes. The random forest classifier randomly draws 1001 decision trees and averages their results in order to provide a low-variance estimator of the probability of detection,  $p_{\text{det}}$ . Each tree is built by sampling the initial list of clusters with replacement. The thresholds at each node of a tree are chosen by minimizing the Gini impurity. The uncertainty on the value of  $p_{\text{det}}$  is obtained with a custom implementation of the unbiased infinitesimal jackknife variance estimator proposed by Wager et al. (2014). Various algorithm parameters are tested and optimized by balancing execution time and classifier scores. Such scores measure the fractional number of objects in the validation subsample that end up correctly classified (with  $p_{\text{det}} = 0.5$  selected as classification threshold). Scores of our classifiers typically reach 80–90%, depending on the nature and the number of selected features. In order to prevent the classifier from extrapolating out of the training zone, we use a simple convex hull algorithm (Barber et al. 1996).

The selection of features relevant for cluster selection functions is based on practical concerns as well as on careful examination of the classifier outcome. Among the variables being tested, the cluster (true) 0.5–2 keV X-ray counts, its flux in the same band, the redshift, mass and luminosity are found to be the most discriminating ones, as it is expected from earlier sensitivity studies. We reform our choice of parameters by examining the feature importance of the random forest classifier and we found that the central emission measure as well as the local exposure time play additional roles on the selection.

The second set of selection functions relies on Gaussian processes (e.g., Rasmussen & Williams 2006). Such a classifier constructs a latent variable, modeled as a Gaussian process whose covariance function (kernel) is a squared exponential function. It is transformed into a probability by means of a sigmoid (inverse probit) function, and the algorithm uses the Bernoulli likelihood of the training sample in order to maximize the marginal likelihood and find the best hyper-parameters for the kernel, namely its amplitude and scale-lengths along each feature dimension. In order to increase speed in execution time, we use the Stochastic Variational Gaussian Process (SVGP) algorithm (Hensman et al. 2015) implemented in the GPy library<sup>6</sup>. Among the additional modeling hypotheses, this algorithm imposes a number of 10 inducing points to create an auxiliary random process summarizing the latent function. The selection probability  $p_{\text{det}}$  is obtained by integrating out the latent variable distribution against the link function (the sigmoid); uncertainties on  $p_{\text{det}}$  are approximated by folding the 1- $\sigma$  envelope of the latent function into the link

<sup>5</sup> Version 0.23.2

<sup>6</sup> GPy, since 2012: A Gaussian process framework in Python; Version 1.9.9; <http://github.com/SheffieldML/GPy>

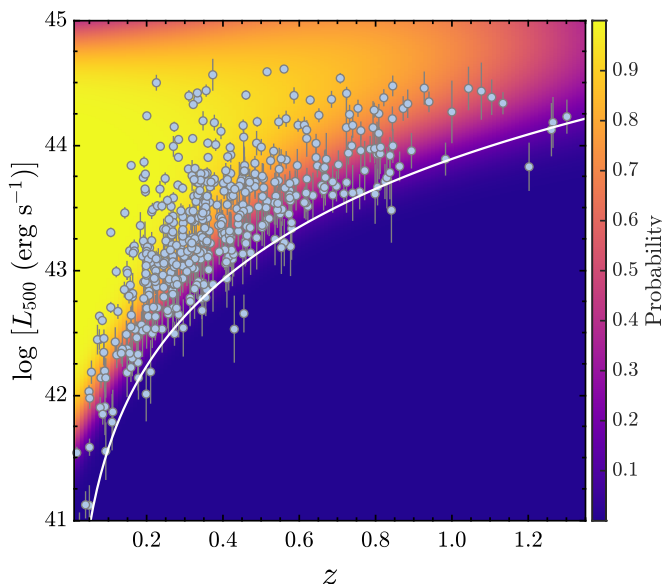


**Fig. 5.** Detection probability as a function of luminosity  $L_{500}$  in the 0.5–2 keV band and redshift  $z$ . The data points with error bars are the  $L_{500}$  for the clusters with  $> 2\sigma$  measurements. Details of the computation of  $L_{500}$  are presented in Sect. 5. The white curve shows the flux limit at  $1.5 \times 10^{-14} \text{ erg s}^{-1} \text{ cm}^{-2}$ , corresponding to an average completeness level of  $\sim 40\%$ .

function. The resulting selection functions appear smoother than those trained with random forests and their uncertainty range is better controlled; however they display increased difficulty in capturing small-scale variations in the feature space. Nevertheless, both flavors of the selection function provide equivalent performances.

In Fig. 5, we show the selection probability as a function of cluster luminosity and redshift using Gaussian processes.

#### 4. X-ray Analysis and Cluster X-ray Properties

In this section we will describe the X-ray analysis on the 542 cluster candidates performed in this work on basis of the PV phase eROSITA observations. The analysis mainly consists of two parts, imaging analysis and spectral analysis, which aim at providing a measurement of cluster average temperature, and the radial profiles of other observables such as flux, luminosity, electron density, and gas mass. As an example, the image, spectrum, and the measured electron density profile of one of the most massive clusters in the field, eFEDS J092121.2+031726, are shown in Fig. 6.

##### 4.1. Imaging analysis, Luminosity, and Gas Mass

The X-ray imaging analysis for the eFEDS field has been extensively described in Ghirardini et al. (2021), we only highlight the major steps here. We note that, in the imaging analysis of this work, we do not conduct further analyses of the morphology and dynamical status of the clusters. An in-depth study of the morphological parameters of the eFEDS clusters will be performed in Ghirardini et al., (submitted.).

The method of imaging analysis in this work is based on a direct image fitting, building a cluster model, projecting it on the plane of the sky and adding to it the model images of instru-

mental and sky backgrounds. Images and exposure maps (both vignetted and unvignetted) are extracted in the soft 0.5–2 keV energy band using the eSASS tools `evtool` and `expmap`.

To model the image for each cluster, we adopted a forward modeling approach. We started from the Vikhlinin et al. (2006) electron number density model:

$$n_e^2(r) = n_0^2 \cdot \left(\frac{r}{r_c}\right)^{-\alpha} \cdot \left(1 + \left(\frac{r}{r_c}\right)^2\right)^{-3\beta+\alpha/2} \cdot \left(1 + \left(\frac{r}{r_s}\right)^3\right)^{-\epsilon/3}, \quad (1)$$

where  $n_0$  is the normalization factor,  $r_c$  and  $r_s$  are core and scale radii,  $\alpha$  controls the slope of the density profile in core and intermediate radii, and  $\epsilon$  controls the change of slope at large radii. The priors on our parameters were  $\epsilon < 5$  (as suggested by Vikhlinin et al. 2006),  $\beta > 1/3$ , and  $\alpha > 0$ , and we froze  $r_s = r_c$ . The number density model was then projected on the 2D image plane, convolved with eROSITA’s PSF and multiplied by the vignetted exposure map. The resulting cluster model image is finally matched to the count image to get the best-fit:

$$S = \frac{1}{4\pi(1+z)^4} \int n_e n_p \Lambda(kT, Z) dl, \quad (2)$$

where  $n_e$  and  $n_p$  are the number density of electron and proton, respectively, and we assume  $n_e = 1.2n_p$ .  $\Lambda(kT, Z)$  is the band averaged cooling function, dependent on temperature and metallicity, and  $dl$  is the integral along the line of sight (Bulbul et al. 2010).

To compute the ICM mass of a cluster from the electron density profile, we use the enclosed ICM mass within a given aperture obtained by integrating the best-fit density model,

$$M_{\text{ICM}} = 4\pi\mu_e m_p \int_0^R n_e(r) r^2 dr, \quad (3)$$

where we assume 0.3 solar abundance of the ICM, adopting the solar abundance table, including the He abundance, from Asplund et al. (2009). The average nuclear charge and mass are  $A \sim 1.4$  and  $Z \sim 1.2$ , and  $\mu_e = A/Z \sim 1.17$ .

The particle background map is obtained by folding the instrumental background parameter to the unvignetted exposure map. The sky-background component, including contribution from the cosmic X-ray background, Galactic Halo, and the Local Bubble, is added to the particle background after being folded by the vignetted exposure map to create the total background model.

The faint point sources within the images are excised, while the bright ones are modeled as delta functions convolved with the PSF to eliminate residual emission due to the wings of the PSF. The resultant model image is fit with the soft band image of eFEDS observations utilizing the Monte Carlo Markov Chain (MCMC) code `emcee` (Foreman-Mackey et al. 2013) to find the best-fit parameters, consisting of parameters of the number density model. We integrate the surface brightness profile and convert it to luminosity and flux by constructing an apec model in Xspec, adopting the ICM temperature measured from the spectral analysis. Clearly, the energy conversion factor (ECF) depends on the temperature which itself varies with radial distance from the cluster center. Taking advantage of the weak dependence of this conversion with temperature (Pacaud et al. 2016), we simply adopt the temperature measured within 500 kpc to compute the ECF for any radius. Both the MCMC chains for spectral and imaging analysis are used to compute the ECF. By integrating the full probability distributions of temperature and

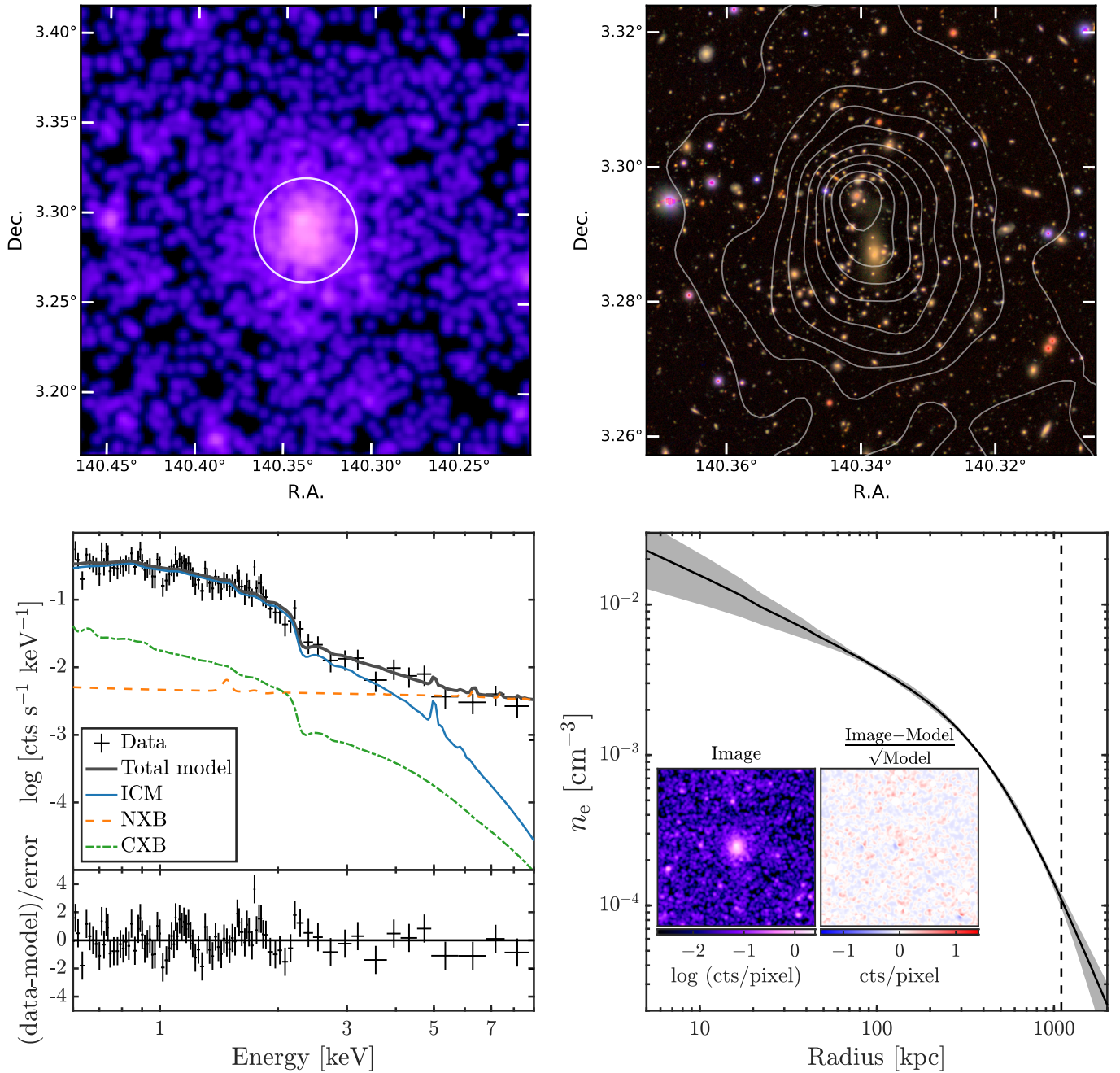


**Fig. 6.** Results of imaging and spectral analysis for cluster eFEDS J092121.2+031726 at redshift 0.333 (spectroscopic) as an example. This cluster is detected with  $\mathcal{L}_{\text{ext}} = 478.6$  and  $\mathcal{L}_{\text{det}} = 1729.8$ , and is one of the clusters with the highest S/N in our sample. The temperature and soft band luminosity within 500 kpc are  $5.2_{-0.8}^{+1.3}$  keV and  $2.14_{-0.08}^{+0.08} \times 10^{44}$  erg s $^{-1}$ . *Upper Left:* Soft band (0.5–2 keV) eROSITA image. The white circle marks the region of  $r = 500$  kpc. The image is smoothed with a Gaussian with FWHM=12''. *Upper right:* Subaru HSC image of the central region in the ( $z, i, r$ ) bands. Superimposed in white color are the X-ray contours. *Lower left:* Spectrum within the 500 kpc region. The spectra and the corresponding responses of the seven TMs are merged only for the sake of a better visualization. The total model, ICM model, non X-ray background, and cosmic X-ray background, are plotted separately. *Lower right:* Electron density profile obtained from the spectral and imaging analysis. The dashed vertical line shows the  $R_{500}$  of this cluster, 1.1 Mpc, estimated from  $L - M$  scaling relation. The inset images show the result of 2-D image fitting, the original soft band image is on the left, while the residual image is on the right.

surface brightness, we self-consistently estimate the uncertainties on both luminosity and flux measurements.

We obtain significant ( $> 2\sigma$ ) luminosity measurements for  $\sim 90\%$  of the clusters, despite that we only obtain temperature measurements with the same significance level for a much lower fraction (see Sect. 4.2). This is due to the fact that the imaging

data is used for measuring the luminosity, and because conversion factor from surface brightness to luminosity has only a weak dependence on temperature. The luminosity-redshift distribution of the eFEDS cluster sample is shown in Fig. 7. For clarity, we only plot the data points with  $> 2\sigma$  significance for each measurement. The figure clearly shows the flux-limited nature of the

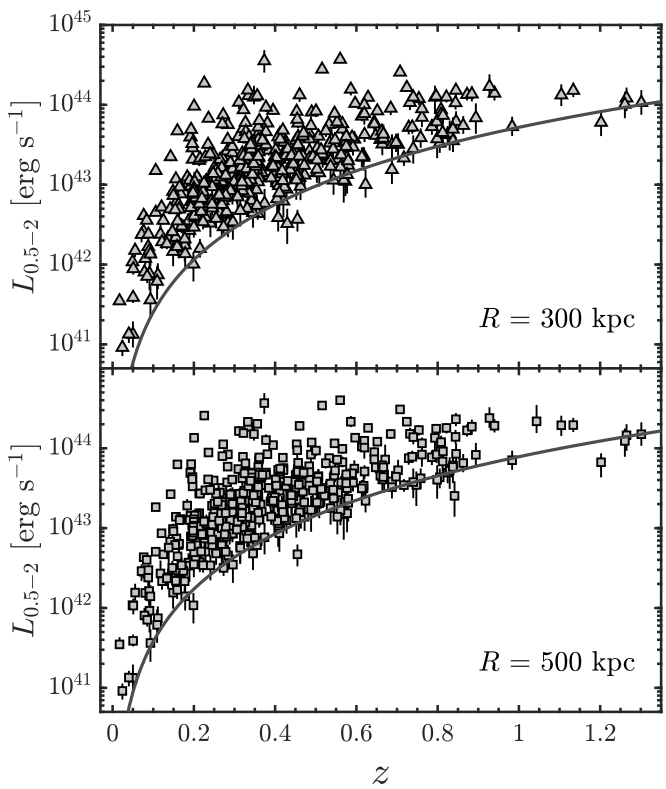


**Fig. 7.** Luminosity redshift distribution of the clusters with significant luminosity measurements ( $> 2\sigma$ ) for 300 kpc (upper panel) and 500 kpc (lower panel). The black curve shows the flux limit:  $10^{-14} \text{ erg s}^{-1} \text{ cm}^{-2}$  for 300 kpc and  $1.5 \times 10^{-14} \text{ erg s}^{-1} \text{ cm}^{-2}$  for 500 kpc (without considering  $K$ -correction).

sample, and the absence of high-luminosity clusters at low redshift due to the small volume, both of which are common for a flux-limited survey such as eFEDS. These biases should be taken into account for further analysis of cosmological parameters and scaling relations.

#### 4.2. Spectral analysis

The spectral extraction and the computing of ancillary response files (ARFs), redistribution matrix files (RMFs) from the seven telescope modules (TMs) are performed using the eSASS algorithm `srctool` with the latest version of the calibration database.

For the extraction radius used for spectral analysis, we opted for two fixed physical apertures, 300 kpc and 500 kpc. The former is chosen to have a fair comparison with similar flux-limited surveys, for instance, the XXL survey (Pacaud et al. 2016). The latter is a compromise between the aim to include more photons and the rapidly decreasing signal-to-noise (S/N) in cluster outskirts. In Fig. 8, we verify the selection of the two extraction radii by plotting the S/N in the soft band as a function of extraction radius. We remark that, while the radius of 300 kpc was determined regardless of the S/N, we do have the majority of the clusters reaching maximum S/N around 500 kpc. We note that due to the wide PSF of the eROSITA mirrors, photons originating from particular regions in the sky may get detected in the adjacent regions on the detector, known as the PSF spilling effect. This effect is particularly important for high-redshift clus-

ters ( $z > 1.5$ ), where the 300 kpc regions are comparable to the 26''FOV-average PSF HEW of eROSITA. Given that we do not have clusters at  $z > 1.5$  in this sample, we omit the systematic uncertainties due to PSF spilling in this work.

The background spectra are extracted within a [2500–4000] kpc annulus centered at each cluster’s centroid, after masking the emission from point sources and other clusters. The inner radius of the background region corresponds to  $\sim 3R_{500}$  for a cluster with  $M_{500} = 2 \times 10^{14} M_\odot$  at  $z = 0.3$ . We check this choice of background radius on the eFEDS image, and confirmed that the inner radius of 2500 kpc extended well beyond the ICM emission in our data for all the clusters. The background spectra include the contribution from unvignetted instrumental background due to galactic cosmic rays (Freyberg et al. 2020) and vignetted cosmic X-ray background due to unresolved point sources, Local Hot Bubble and Galactic Halo emission. Our final total background model then includes an unabsorbed apec model for the Local Hot Bubble and two absorbed apec models for the Galactic halo and the Local Group at  $\sim 0.25$  keV and at a slightly higher temperature at  $\sim 0.75$  keV (Kuntz & Snowden 2000; Snowden et al. 2008; Bulbul et al. 2012). The cosmic X-ray background due to unresolved sources is modeled by an absorbed power-law, where the index is frozen to 1.46 (see, e.g., Luo et al. 2017) and the normalization is determined by fitting the local background spectra. The fitting band was restricted to 0.8–9 keV for the TMs affected by the light leak (TM5 and TM7, see Predehl et al. 2021), while the 0.6–9 keV spectrum was used for all the other TMs. A more conservative way to get rid of the light leak is to totally ignore the spectra of TMs 5 and 7. However, this will lose a significant fraction of good photons, and further reduce the S/N. We compare our fitting results with those obtained by ignoring TMs 5 and 7 for a sample of 50 clusters with the highest S/N. We find that the temperatures measured with and without TMs 5 and 7 are consistent within  $1\sigma$  statistical uncertainty for all the cases. The normalization of spectra of TMs 5 and 7 is more affected by the calibration issues and light leak. However, we find that the difference in normalization with and without TMs 5 and 7 is also within  $2\sigma$ . Since the electron number density and luminosity are not directly determined from the spectroscopy (and the normalization) but from the imaging analysis, we do not expect that our measurements are significantly affected by calibration issues related to TMs 5 and 7. We therefore decide to keep TMs 5 and 7 in the spectral fitting, and only ignore the energy range below 0.8 keV, as already mentioned.

Since we are in the low-count regime in most of our detected clusters, we strictly used C-statistics in our fits (Cash 1979) and modeled our background instead of subtracting it from the total spectrum. The ICM emission is fit with the apec thermal plasma emission model (Smith et al. 2001; Foster et al. 2012). The solar abundance table from Asplund et al. (2009) is adopted. The Galactic hydrogen absorption is modeled using tbabs (Wilms et al. 2000), where the column density  $n_H$  is fixed to  $n_{H,\text{tot}}$  provided by Willingale et al. (2013) at the cluster position. This value takes not only the neutral hydrogen into account, but also the molecular hydrogen. The current version of the tbabs model includes the most accurate atomic data available for neutral species (e.g., they consider the smearing of the K-photoabsorption edge via Auger decay)<sup>7</sup>. The spectral fitting was done using Xspec version 12.11.1 (Arnaud 1996).

Due to the shallow depth of the eFEDS survey, we do not have significant metallicity measurements for all clusters in the

<sup>7</sup> <https://pulsar.sternwarte.uni-erlangen.de/wilms/research/tbabs>

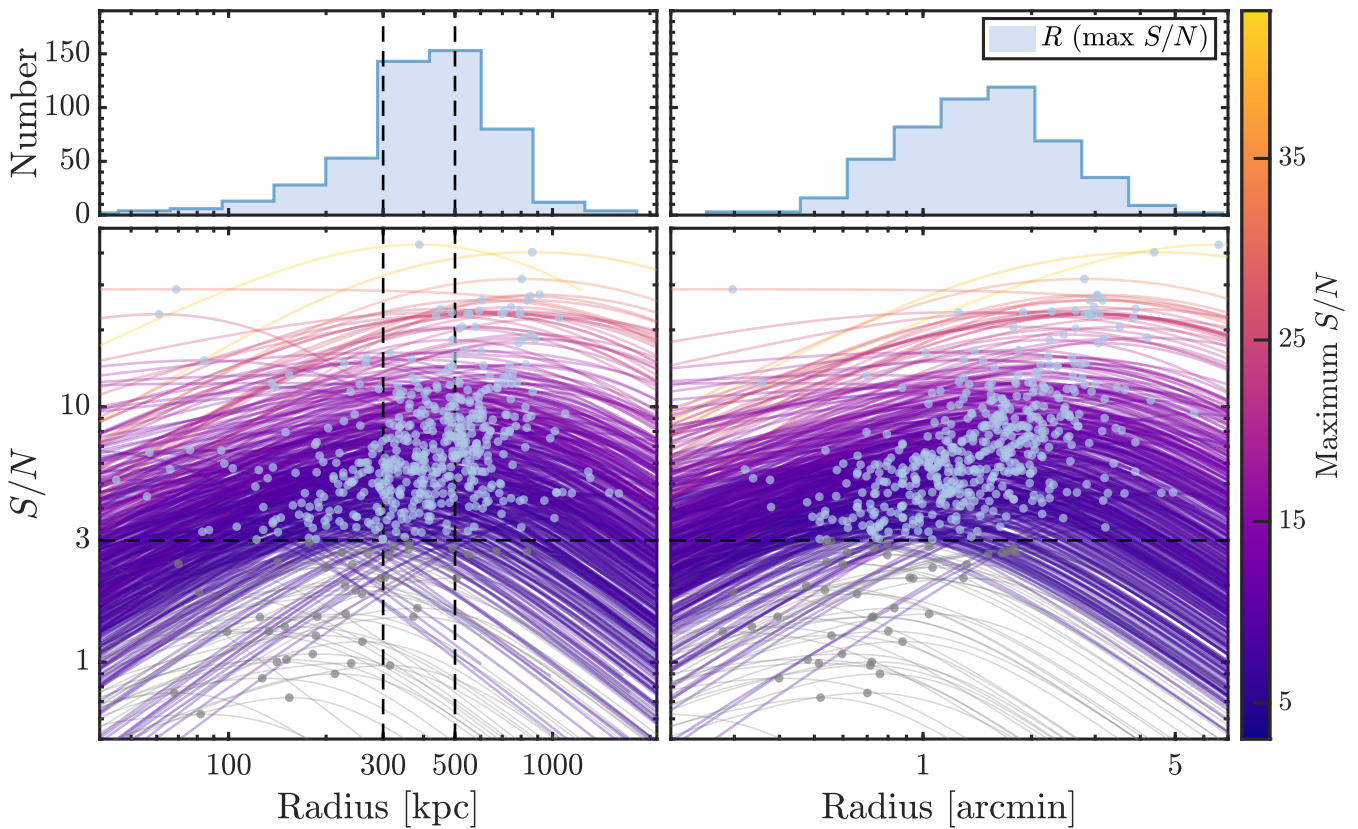


**Fig. 8.** Signal to noise ratio profiles for all the clusters. The net count rates are computed from the best-fit model of the soft band image (see Sect. 4.1 for more details). For each cluster, the S/N as a function of radius is shown as a curve color-coded by its maximum value. The maximum S/N and the corresponding radii for all clusters are marked with blue dots. Clusters with maximum S/N lower than 3 are plotted in dark gray. The histogram in the upper-left panel shows the distribution of the maximum S/N, only considering clusters with maximum S/N higher than 3, in order to get rid of the contamination from low-significance clusters.

sample (see Fig. 6 for example). Therefore, we fix the metallicity to  $0.3 Z_{\odot}$  (see, e.g., Liu et al. 2020) for all clusters for a uniform treatment of the data. The redshift of the cluster is set at the value provided by MCMF, as described in Sect. 2.3. We use spectroscopic redshifts where available, and adopt photometric redshifts for the rest of the clusters. We note that the redshifts of the ICM and member galaxies may be slightly different, especially in disturbed clusters (e.g., Liu et al. 2015), therefore, an ideal approach is to allow the redshift to vary within a small range. However, given the low number of photons in our spectra (only a few clusters in our sample have  $\sim 1000$  net counts in the full band within 500 kpc), for the vast majority of the sample, we are not able to obtain a significant constraint on redshift from the X-ray spectral analysis. Thawing the redshift in the model does not improve the spectral fitting. We, therefore, fix the redshift parameter to the MCMF values mentioned above for all the clusters. Moreover, the measurement of redshift from X-ray spectra requires well-understood gain calibration of the CCD (see, e.g., Sanders et al. 2020). Therefore, we will explore the X-ray redshift determination in future studies. We also note that we ignore the multiple phase nature of the ICM within our extraction radii by using a single apec model in the spectral fitting. This would unavoidably result in larger residual particularly in the soft band (see Fig. 6, lower left panel). However, considering the low S/N in our data, we argue that an averaged spectroscopic-like temperature is the only quantity we can measure, and that constraining

the multi-temperature structures in the ICM is well beyond the data quality and the goal of this paper.

Due to the shallow survey data, we are not able to obtain a robust constraint on temperature for most of the clusters where we only detected less than 100 counts in the 0.5–2 keV band within 500 kpc. Another problem in temperature measurement is the contamination of misidentified AGN in the sample. Finally, we were able to measure accurate temperatures of only 102 clusters ( $\sim 1/5$  of the full sample) at  $> 2\sigma$  significance level. All these clusters have  $> 100$  counts in the 0.5–2 keV band within 500 kpc. Most of them (100/102) have  $L_{\text{ext}} > 10$ , thus the contamination level of this subsample is much lower than the average of the full sample. We plot the  $L - T$  relations for 300 kpc and 500 kpc in Fig. 9. The ICM temperature of these 102 clusters ranges from  $\sim 0.5$  keV to  $\sim 7$  keV, and the average temperature is  $\sim 2$  keV, implying that they are dominated by low-mass clusters and groups (see, e.g., Born et al. 2014, Fig. 3). As expected owing to the large effective area in the soft band, we are more sensitive to low-mass cluster and group populations compared to other surveys. Moreover, our ability to measure hot clusters at  $> 5$  keV is limited due to eROSITA’s reduced sensitivity in the energy band  $> 3$  keV. It is clearly reflected on Fig. 9 as the ICM temperatures of hot clusters are not well constrained. It can also be noted on Fig. 9 that several outliers appear at high luminosity but relatively low temperature. For example, eFEDS J083812.0-015934, eFEDS J092339.0+052655, and eFEDS J093521.0+023234 have  $L_{0.5-2 \text{ keV}, 300 \text{ kpc}} = 3.70^{+0.34}_{-0.31} \times$

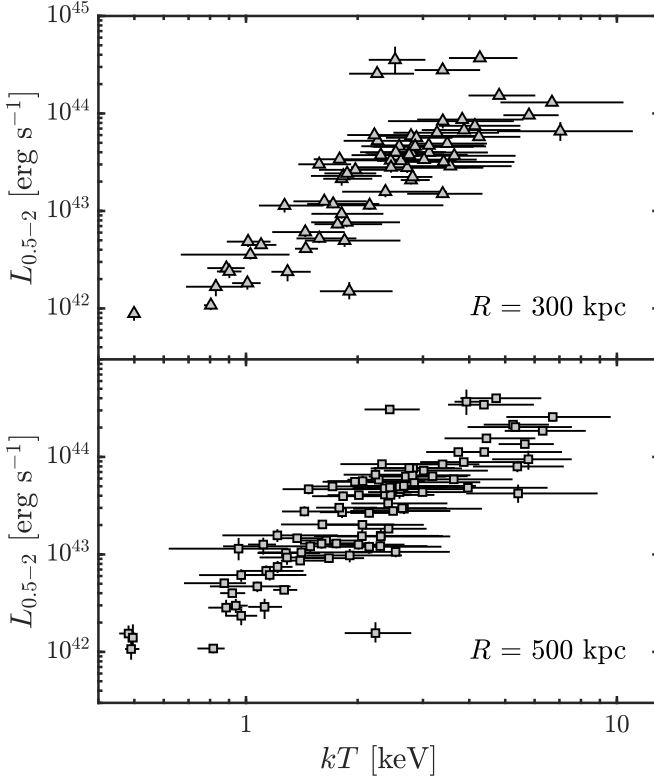


**Fig. 9.** Luminosity plotted as a function of temperature for the clusters with  $>2\sigma$  temperature measurements in either of the two radii.

$10^{44}$ ,  $3.55_{-1.02}^{+1.30} \times 10^{44}$ , and  $2.79_{-0.19}^{+0.17} \times 10^{44}$  erg s $^{-1}$ , and  $kT_{300 \text{ kpc}} = 4.27_{-0.74}^{+1.12}$ ,  $2.52_{-0.38}^{+0.53}$ , and  $3.39_{-0.54}^{+0.89}$  keV. We carefully check the X-ray and optical data for these cases, and find that they are all massive clusters, with estimated  $R_{500}$  (see Sect. 5) of  $> 1.2$  Mpc, much larger than the 300 kpc and 500 kpc extraction radii we choose. The low temperatures we measured are probably due to the cool core which dominates the emission within our extraction radii. This also reminds us that a meaningful research on the relations between the X-ray observables can only be made after an accurate measurement of the  $R_{500}$  of the clusters, from which both the core-included and core-excluded X-ray observables can be measured. The detailed study of the scaling relations between different X-ray observables, for example,  $L-T$  and  $L-M_{\text{gas}}$  measured within  $R_{500}$ , will be performed in a future work by Bahar et al., (in prep.).

We provide in Table B.2 the main X-ray observables of the 102 clusters with  $>2\sigma$  temperature measurements within either 300 kpc or 500 kpc. The full table containing the X-ray analysis results of all the 542 clusters is available at <https://erosita.mpe.mpg.de/edr/eROSITAObservations/Catalogues>.

## 5. X-ray Luminosity Function

The X-ray luminosity function (XLF) of a galaxy cluster survey is defined as the count of clusters per effective survey volume as a function of cluster luminosity. A widely adopted strategy is to measure XLF by dividing the cluster sample into luminosity bins (see Böhringer et al. 2014, for example), the XLF can be written

**Table 3.** X-ray luminosity function of the eFEDS clusters for the full sample and in two redshift bins.

$L_{500}$	$dn/dL$	$-1\sigma$	$+1\sigma$
$0.01 < z < 1.3$			
$0.96_{-0.46}^{+0.58}$	$3.29 \times 10^{-3}$	$1.76 \times 10^{-3}$	$5.06 \times 10^{-3}$
$1.93_{-0.39}^{+0.33}$	$8.10 \times 10^{-4}$	$3.08 \times 10^{-4}$	$1.35 \times 10^{-3}$
$2.83_{-0.58}^{+0.45}$	$5.35 \times 10^{-4}$	$2.67 \times 10^{-4}$	$8.19 \times 10^{-4}$
$4.07_{-0.79}^{+0.71}$	$2.76 \times 10^{-4}$	$1.54 \times 10^{-4}$	$4.11 \times 10^{-4}$
$5.55_{-0.77}^{+1.42}$	$1.38 \times 10^{-4}$	$8.64 \times 10^{-5}$	$1.96 \times 10^{-4}$
$8.40_{-1.44}^{+1.75}$	$6.79 \times 10^{-5}$	$4.52 \times 10^{-5}$	$9.22 \times 10^{-5}$
$12.74_{-2.59}^{+2.04}$	$3.09 \times 10^{-5}$	$2.21 \times 10^{-5}$	$4.07 \times 10^{-5}$
$17.75_{-2.97}^{+3.79}$	$1.22 \times 10^{-5}$	$8.93 \times 10^{-6}$	$1.62 \times 10^{-5}$
$26.45_{-4.91}^{+4.93}$	$5.47 \times 10^{-6}$	$3.95 \times 10^{-6}$	$7.29 \times 10^{-6}$
$38.11_{-6.73}^{+7.60}$	$2.30 \times 10^{-6}$	$1.73 \times 10^{-6}$	$2.98 \times 10^{-6}$
$54.67_{-8.96}^{+11.93}$	$8.61 \times 10^{-7}$	$6.68 \times 10^{-7}$	$1.10 \times 10^{-6}$
$79.67_{-13.07}^{+17.35}$	$2.52 \times 10^{-7}$	$1.70 \times 10^{-7}$	$3.53 \times 10^{-7}$
$108.37_{-11.35}^{+32.98}$	$7.02 \times 10^{-8}$	$4.59 \times 10^{-8}$	$9.98 \times 10^{-8}$
$163.34_{-22.00}^{+42.58}$	$2.73 \times 10^{-8}$	$1.91 \times 10^{-8}$	$3.62 \times 10^{-8}$
$239.08_{-33.16}^{+60.92}$	$1.04 \times 10^{-8}$	$7.31 \times 10^{-9}$	$1.39 \times 10^{-8}$
$0.01 < z < 0.35$			
$0.99_{-0.49}^{+0.63}$	$3.03 \times 10^{-3}$	$1.72 \times 10^{-3}$	$4.60 \times 10^{-3}$
$2.30_{-0.68}^{+0.63}$	$6.03 \times 10^{-4}$	$3.44 \times 10^{-4}$	$9.02 \times 10^{-4}$
$4.10_{-1.18}^{+1.16}$	$2.11 \times 10^{-4}$	$1.38 \times 10^{-4}$	$2.95 \times 10^{-4}$
$7.39_{-2.12}^{+2.10}$	$6.68 \times 10^{-5}$	$4.93 \times 10^{-5}$	$8.49 \times 10^{-5}$
$12.42_{-2.92}^{+4.68}$	$2.64 \times 10^{-5}$	$2.21 \times 10^{-5}$	$3.07 \times 10^{-5}$
$21.37_{-5.94}^{+9.44}$	$8.30 \times 10^{-6}$	$6.74 \times 10^{-6}$	$9.85 \times 10^{-6}$
$40.26_{-9.45}^{+15.24}$	$2.81 \times 10^{-6}$	$2.16 \times 10^{-6}$	$3.44 \times 10^{-6}$
$62.31_{-6.80}^{+37.69}$	$6.13 \times 10^{-7}$	$3.97 \times 10^{-7}$	$8.13 \times 10^{-7}$
$0.35 < z < 1.3$			
$12.91_{-2.91}^{+1.68}$	$3.38 \times 10^{-5}$	$1.86 \times 10^{-5}$	$4.97 \times 10^{-5}$
$18.19_{-3.60}^{+3.10}$	$1.25 \times 10^{-5}$	$8.15 \times 10^{-6}$	$1.75 \times 10^{-5}$
$25.53_{-4.24}^{+5.54}$	$5.36 \times 10^{-6}$	$3.48 \times 10^{-6}$	$7.28 \times 10^{-6}$
$37.01_{-5.94}^{+8.33}$	$2.29 \times 10^{-6}$	$1.63 \times 10^{-6}$	$3.07 \times 10^{-6}$
$53.23_{-7.89}^{+12.93}$	$8.40 \times 10^{-7}$	$6.14 \times 10^{-7}$	$1.09 \times 10^{-6}$
$78.67_{-12.51}^{+17.88}$	$2.49 \times 10^{-7}$	$1.64 \times 10^{-7}$	$3.56 \times 10^{-7}$
$107.43_{-10.89}^{+33.45}$	$6.69 \times 10^{-8}$	$4.24 \times 10^{-8}$	$9.61 \times 10^{-8}$
$159.54_{-18.65}^{+46.05}$	$2.63 \times 10^{-8}$	$1.76 \times 10^{-8}$	$3.55 \times 10^{-8}$
$245.82_{-40.24}^{+54.18}$	$8.60 \times 10^{-9}$	$5.49 \times 10^{-9}$	$1.18 \times 10^{-8}$

**Notes.**  $L_{500}$  are in units of  $10^{42}$  erg s $^{-1}$ . Luminosity function values are in units of [ $\text{Mpc}^{-3}$  ( $10^{44}$  erg s $^{-1}$ ) $^{-1}$ ].

as:

$$\frac{dn}{dL}(\langle L_i \rangle) = \frac{1}{\Delta L_i} \sum_j \frac{1}{V_{\text{eff}}[L_j, F_{\text{lim}}, A(F_j)]/P(L_j, z_j)}, \quad (4)$$

where  $\langle L_i \rangle$  and  $\Delta L_i$  are the center luminosity (in this work we use  $L_{500}$  in 0.5–2 keV) and the width of the  $i^{\text{th}}$  luminosity bin,  $L_j$  is the luminosity of the  $j^{\text{th}}$  cluster in the  $i^{\text{th}}$  bin.  $P(L_j, z_j)$  is the detection probability of a cluster with luminosity  $L_j$  at redshift  $z_j$ , obtained from the selection function (see Sect. 3).  $V_{\text{eff}}[L_j, F_{\text{lim}}, A(F_j)]$  is the survey effective volume as a function of  $L_j$  and the flux limit and sky coverage of the survey. The flux limit is set as  $F_{\text{lim}} = 1.5 \times 10^{-14}$  erg s $^{-1}$  cm $^{-2}$  (see Fig. 5). Since the exposure is nearly uniform across the whole eFEDS field above the flux limit, we used a constant sky coverage  $A = 126$  deg $^2$ , determined as the sky area with vignetted exposure larger than 0.5 ks, which is the lowest exposure where a cluster with flux close to the flux limit is detected.  $V_{\text{eff}}$  is then

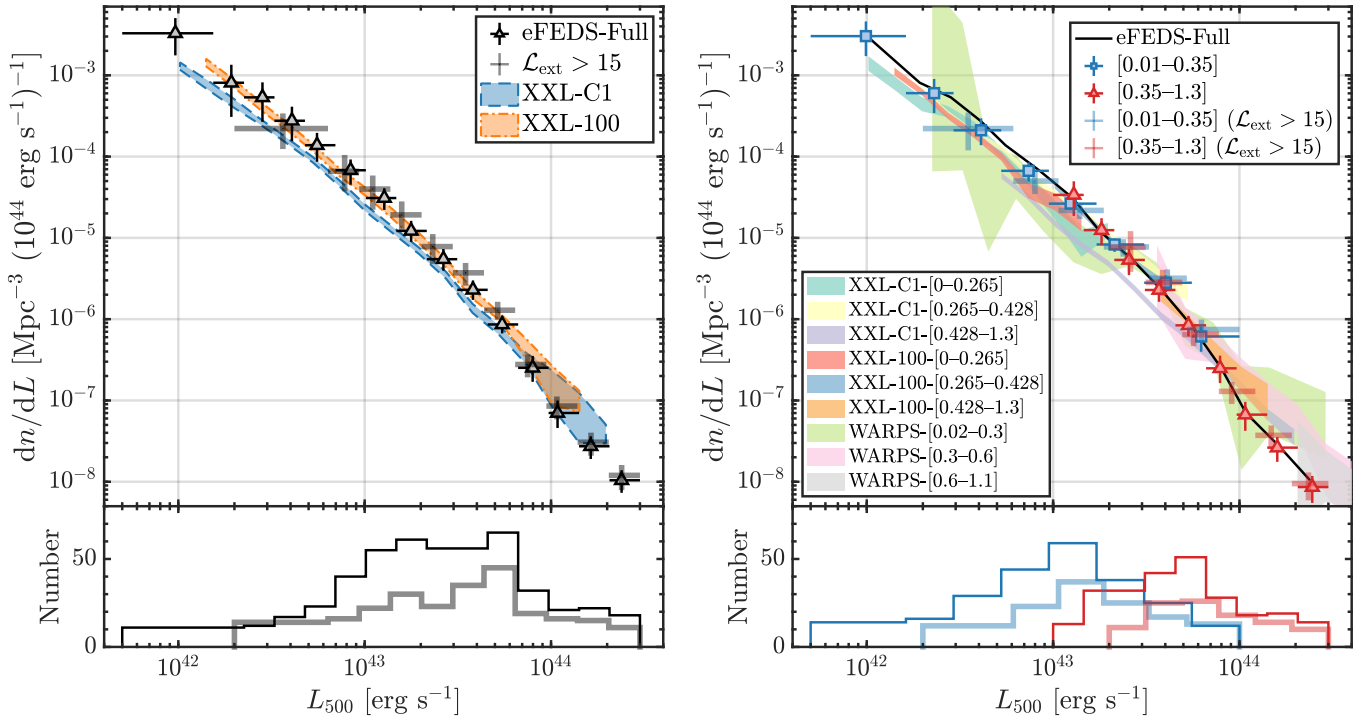


**Fig. 10.** X-ray luminosity function of the eFEDS cluster sample. *Left panel:* Results for the full sample. *Right panel:* Results in two redshift bins. The number of clusters in each bin is indicated in the lower panel. Some literature results are plotted as shaded area for comparison: XXL-C1 (Adami et al. 2018), XXL-100 (Pacaud et al. 2016), WARPS (Koens et al. 2013). Thick errorbars show the results of the  $\mathcal{L}_{\text{ext}} > 15$  subsample.

computed as the co-moving shell volume between redshift 0 and the redshift where the cluster can be detected at the flux limit, scaled by the sky coverage. Since our sample has an average contamination fraction of  $\sim 1/5$ , we finally scale the  $dn/dL$  by a factor of 0.8.

To be able to calculate the XLF of the eFEDS sample, the luminosity  $L_{500}$  measured within  $R_{500}$  must be known. There are several ways to measure the mass, thus computing the  $R_{500}$ , for a cluster, such as a dedicated weak-lensing analysis (see Umetsu 2020, for a review), and a measurement of hydrostatic mass on basis of deeper X-ray observation (see, e.g., Ettori et al. 2019). In this work we estimate the  $R_{500}$  in another way: the  $R_{500}$  of each cluster is determined as the radius within which the mass  $M_{500}$  and luminosity  $L_{500}$  are consistent with cluster  $L - M$  scaling relation. While the majority of the published  $L - M$  scaling relations in the literature focus on massive clusters (e.g., Pratt et al. 2009; Vikhlinin et al. 2009; Bulbul et al. 2019; Andrade-Santos et al. 2021), a few studies also involved the lower end of the mass scale (see, e.g., Eckmiller et al. 2011; Lovisari et al. 2015; Sereno et al. 2020). Since the eFEDS sample consists of mostly low-mass clusters, we adopt the Lovisari et al. (2015)  $L - M$  scaling relation, which is based on an X-ray selected bias-corrected sample of 20 galaxy groups and 62 massive HIFLUGCS clusters. We note that in their work, Lovisari et al. (2015) calculate the masses based on X-ray data and hydrostatic equilibrium assumption. The value of  $R_{500}$  obtained from this approach is just a rough estimation. We will discuss the impact of the choice of

scaling relations on our results in Sect. 5.1. The Lovisari et al. (2015)  $L - M$  relation is:

$$\log\left(\frac{L_{0.1-2.4}}{10^{43} h_{70}^{-2} \text{ erg s}^{-1}}\right) = 1.39 \times \log\left(\frac{M_{500}}{5 \times 10^{13} h_{70}^{-1} M_{\odot}}\right) - 0.12, \quad (5)$$

where  $L_{0.1-2.4}$  is the luminosity in 0.1–2.4 keV energy range within  $R_{500}$ , and is computed for each cluster in our sample using the same method described in Sect. 4.1. We note that the 0.1–2.4 keV band luminosity is only used to estimate  $R_{500}$  with the above scaling relation. We use 0.5–2 keV band luminosity in the computing of luminosity function.

The luminosity range  $[5 \times 10^{41} - 3 \times 10^{44}] \text{ erg s}^{-1} \text{ cm}^{-2}$  is divided into several bins with equal logarithmic width. The bins at low- $L$  and high- $L$  edges are then slightly adjusted in order to make sure that each bin includes at least 10 clusters. The center of each bin is determined as the weighted-average luminosity of the clusters within it. The errors in  $dn/dL$  are computed from 1000 bootstrapped samples where the luminosity of each cluster is randomized considering the statistical uncertainty. This error is then added in quadrature with the Poisson error for the number of clusters in each bin. We investigate the evolution of XLF by splitting the sample in two redshift bins, 0.01–0.35, and 0.35–1.3, each including  $\sim 250$  clusters. XLFs of the full sample and the two redshift bins are listed in Table 3, and plotted in Fig. 10.

The XLF of galaxy clusters are available in the literature for a variety of samples (see, e.g., Rosati et al. 1998; Vikhlinin et al. 1998; De Grandi et al. 1999; Allen et al. 2003; Mullis et al. 2004; Böhringer et al. 2007; Koens et al. 2013; Böhringer et al. 2014; Pacaud et al. 2016; Adami et al. 2018; Finoguenov et al. 2020).

Here we compare our XLF with the results in several recent works based on different cluster samples, namely the WARPS (Koens et al. 2013), the XXL-100 (Pacaud et al. 2016), and the XXL-C1 (Adami et al. 2018). The comparison is shown in Fig. 10. We find good agreement in the XLFs of the full eFEDS sample and of the XXL-100 and XXL-C1 clusters. In particular, the eFEDS XLF is relatively closer to the result based on the XXL-100 sample, especially for low luminosities. By dividing the eFEDS cluster sample into two redshift bins, we do not observe any significant evolution of the XLF with redshift, consistent with the literatures shown in the right panel of Fig. 10). However, we note that the contamination in the full eFEDS sample at different luminosity and redshift bins may induce a bias in the XLF measurements. Therefore, we also compute the XLF with a purer subsample, obtained by selecting the eFEDS clusters with extent likelihood  $\mathcal{L}_{\text{ext}} > 15$ . This subsample contains  $\sim 250$  clusters in the luminosity range where the XLF is computed, with an estimated purity  $> 90\%$ . The selection function is also recomputed for this subsample according to the corresponding thresholds. As a result, the XLF of the subsample is fully consistent with that of the full sample, as shown in Fig. 10).

### 5.1. The impact of scaling relation on luminosity function

Since the  $R_{500}$  and  $L_{500}$  are determined using  $L - M$  scaling relation, the XLF is dependent on the choice of  $L - M$  relation we adopt. In this section we will assess this effect by comparing the current XLF with the result we obtain with other  $L - M$  relations. The general form of cluster  $L - M$  relation reads  $\log(L) = a \cdot \log(M) + b$ , where the slope  $a$  varies in the range [1, 2] in different works, depending on the cluster population they study (Pratt et al. 2009; Arnaud et al. 2010; Giordini et al. 2013; Lovisari et al. 2015; Bulbul et al. 2019; Sereno et al. 2020). Several works have found that the  $L - M$  relation for galaxy groups is steeper than for massive clusters (see, e.g., Lovisari et al. 2015). This adds the complexity in our selection of  $L - M$  relation for our sample, which includes both low-mass groups and clusters. Despite that we finally chose the result in Lovisari et al. (2015) based on a combined sample of groups and clusters, with  $a = 1.39$ , it is necessary to examine the result when we adopt a steeper relation. We therefore recompute the  $R_{500}$ ,  $L_{500}$ , and the corresponding XLF using the scaling relation in Bulbul et al. (2019):

$$\frac{L_{500}}{10^{44} \text{ erg s}^{-1}} = 4.12 \times \left( \frac{M_{500}}{M_{\text{piv}}} \right)^{1.89} \cdot \left( \frac{E(z)}{E(z_{\text{piv}})} \right)^2 \cdot \left( \frac{1+z}{1+z_{\text{piv}}} \right)^{-0.2}, \quad (6)$$

where  $L_{500}$  is the 0.5–2 keV band luminosity within  $R_{500}$ ,  $M_{\text{piv}} = 6.35 \times 10^{14} M_{\odot}$  and  $z_{\text{piv}} = 0.45$ . We found that, while the large difference in the slopes of the two scaling relations (1.39 and 1.89) changed the  $R_{500}$  by around 10 percent on average, the value of  $L_{500}$  was only affected by a few percent. The XLFs are also in good agreement. Clearly, the cluster sample based on which the scaling relation is obtained in either Lovisari et al. (2015) or Bulbul et al. (2019) does not fit perfectly with the cluster population in our sample, thus preventing us from having a more precise assessment of this bias. The accurate measurements of the quantities  $R_{500}$ ,  $L_{500}$ , and  $M_{500}$ , of these clusters, will have to rely on weak lensing analysis with high quality<sup>8</sup>, or hydrostatic mass measurement on basis of deeper X-ray observations.

<sup>8</sup> Before submitting this paper, we obtained the mass  $M_{500}$  derived from the (count rate - mass - redshift) scaling relation with weak lensing

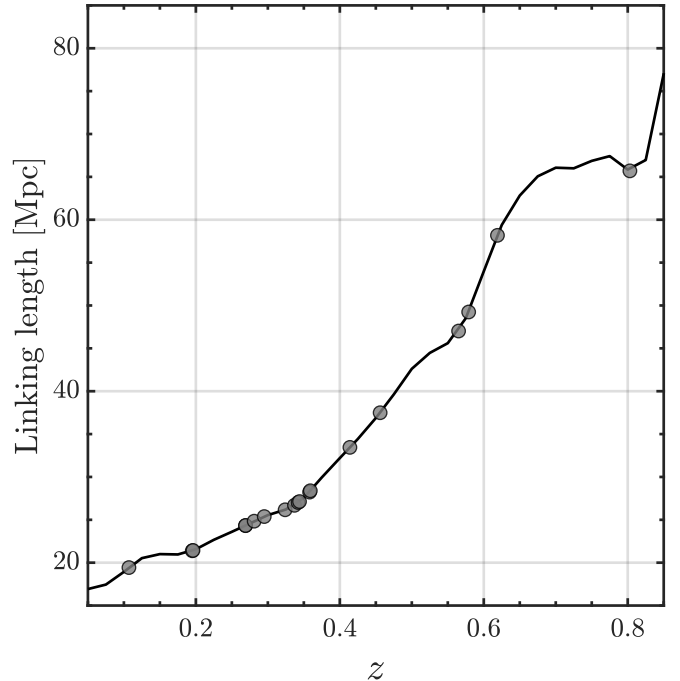


**Fig. 11.** Linking length, in co-moving distances, as a function of cluster redshift in our sample. The circles mark the positions of the 19 supercluster candidates we detected.

## 6. Superclusters in the eFEDS Field

With our sample of 542 galaxy clusters, we further analyze their spatial distribution to search for superclusters. Early supercluster searches used optically detected catalogs of galaxy clusters such as Abell/ACO clusters (see, e.g., Zucca et al. 1993; Einasto et al. 1994). The first supercluster catalog based on X-ray selected clusters was presented in Einasto et al. (2001), where 19 superclusters with multiplicity<sup>9</sup>  $\geq 2$  were detected based on the early RASS catalog. In recent years, more superclusters have been discovered thanks to the increase in the volume and depth of X-ray cluster samples. For instance, Chon et al. (2013) detected 164 superclusters with  $N_{\text{cl}} \geq 2$  at  $z \leq 0.4$  based on the ROSAT-ESO FluxLimited X-ray (REFLEX II) cluster catalog. Adami et al. (2018) detected 35 superclusters with  $N_{\text{cl}} \geq 3$ , and 39 cluster pairs, out to  $z \sim 0.8$ , based on the 365 cluster catalog from the XXL survey.

In this work, we employ a Friends-of-Friends (FoF) algorithm to identify superclusters with an evolving linking length, a method that has been widely used in previous works (Zucca et al. 1993; Einasto et al. 2001; Chon et al. 2013; Chow-Martínez et al. 2014; Adami et al. 2018). This method is well suited to detect superclusters, as they are not virialized objects, thus often have irregular shapes. Our FoF algorithm starts by searching for neighboring clusters (namely, “friends”) with a distance smaller than the linking length for a cluster in the sample. Then for each of the “friends”, the algorithm continues to search for “friends of friends” until no new “friends” can be found. Since the linking length varies with cluster redshift, to make sure that the search

calibration, which will be presented in detail in Chiu et al., (submitted). The  $L_{500}$  are only different by less than a few percent with respect to our results, and the change in the XLF is negligible.

<sup>9</sup> The multiplicity ( $N_{\text{cl}}$ ) of a supercluster is defined as the number of its member clusters.

**Table 4.** Supercluster candidates detected in the eFEDS field.

ID	RA [deg]	Dec [deg]	$N$	$z$	$l(z)$ [Mpc]	$M_{\text{tot}}$ [ $10^{15} M_{\odot}$ ]	$C$
eFEDS-SC1	133.622	+1.201	4	0.107	19.43	0.4	1
eFEDS-SC2	132.914	+0.729	6	0.195	21.39	1.2	0.77
eFEDS-SC3	135.091	+3.009	10	0.196	21.43	3.1	0.58
eFEDS-SC4	140.535	+3.959	5	0.269	24.32	1.6	0.83
eFEDS-SC5	129.959	-1.700	7	0.269	24.34	1.9	0.83
eFEDS-SC6	140.066	+2.483	4	0.281	24.84	1.7	1
eFEDS-SC7	135.390	-1.209	4	0.295	25.38	0.9	1
eFEDS-SC8	133.289	+1.397	4	0.324	26.17	1.0	0.57
eFEDS-SC9	141.682	-1.053	6	0.337	26.69	1.8	0.44
eFEDS-SC10(*)	130.690	+1.045	4	0.342	27.02	0.8	0.86
eFEDS-SC11	143.707	+0.076	4	0.344	27.13	1.3	0.72
eFEDS-SC12	143.862	+0.641	4	0.358	28.23	3.0	1
eFEDS-SC13	129.688	+2.145	4	0.359	28.39	2.0	1
eFEDS-SC14	130.666	+1.226	8	0.414	33.45	2.6	0.49
eFEDS-SC15	138.423	+3.922	4	0.456	37.49	2.3	1
eFEDS-SC16(*)	129.502	-2.060	6	0.565	47.02	4.4	0.77
eFEDS-SC17(*)	140.134	+4.198	4	0.579	49.24	2.5	0.68
eFEDS-SC18(*)	137.574	+3.182	4	0.619	58.18	2.1	0.65
eFEDS-SC19(*)	136.418	+2.489	7	0.803	65.70	5.2	0.49

**Notes.** We mark with (\*) the superclusters where more than half of the members do not have available spectroscopic redshifts. The coordinates and redshifts are the mean values of the member clusters.  $C$  is the compactness, see text for more details.

result is stable, we use the average linking length of the two clusters when computing their relationship.

The linking length of the FoF algorithm, in co-moving distances, can be computed as following (see, e.g., Chon et al. 2013, Eqs. 1–3):

$$l = \left( \frac{N(z_{\min}, z_{\max})}{V(z_{\min}, z_{\max}, A)} \cdot f \right)^{-1/3}, \quad (7)$$

where  $N$  is the number of clusters in the redshift bin,  $V$  is the co-moving volume of the shell, as a function of the lower- and upper- bounds of the bin and the eFEDS survey area  $A$ .  $f$  is the over-density factor. Therefore, the linking length at a specific redshift corresponds to the maximum distance between two clusters defining a region  $f$  times over-dense with respect to the average cluster number density at that redshift. The resulting linking length evolves with the redshift distribution of clusters, and allows us to detect similar over-densities throughout the redshift range. In this work, we set  $\Delta z = 0.05$  and  $f = 10$ , as commonly used in previous works. In Fig. 11, we plot the linking length as a function of cluster redshift in our sample. The linking length increases from  $\sim 20$  Mpc at low- $z$  to  $> 50$  Mpc at high- $z$ , due to the low number density of high- $z$  clusters in our catalog (see Fig. 3).

We classify the cluster systems found by the FoF algorithm with at least 4 members as supercluster candidates. Clearly, systems with 2 or 3 member clusters are also possible objects of interest, and the thresholds of supercluster multiplicity are usually smaller than 4 (e.g., Chon et al. 2013; Adami et al. 2018). However, our cluster sample has a contamination fraction of  $\sim 1/5$ , which decreases the reliability of the superclusters with a low multiplicity. We therefore determine  $N_{\text{cl}} \geq 4$  as our threshold. It can also be observed in Fig. 11 that the linking length starts to increase abnormally beyond redshift  $z \sim 0.8$ . Clearly, the density of clusters at such high redshift in our sample is too low to de-

tect superclusters. We therefore set an upper limit on the linking length:  $l_{\text{max}} = 70$  Mpc, to avoid fake detections at high redshifts.

With the above approach, we detected 19 supercluster candidates in the eFEDS field, listed in Table 4. Multiplicities of these 19 superclusters range from 4 to 10. The cut-out X-ray images of these superclusters and the properties of their member clusters are provided in the Appendix (see Table B.1 and Fig. B.1). The galaxy density maps from the HSC-SSP survey data at the corresponding redshifts for all the superclusters are presented in Fig. B.2. We find a good association between the galaxy density maps and the X-ray images of the superclusters. Moreover, we also identified 46 and 14 cluster systems with 2 and 3 member clusters, respectively. As a comparison, Adami et al. (2018) detected 39 cluster pairs and 35 superclusters with  $N_{\text{cl}} > 3$  in the XXL-365 cluster catalog. Considering the difference between eFEDS and XXL in sky coverage ( $140 \text{ deg}^2$  vs.  $50 \text{ deg}^2$ ), sample size (542 vs. 365), and flux limit ( $10^{-14} \text{ erg s}^{-1} \text{ cm}^{-2}$  vs. a few  $10^{-15} \text{ erg s}^{-1} \text{ cm}^{-2}$ ), we do not find significant inconsistency between the number of superclusters in eFEDS and XXL.

We estimated the mass for each supercluster by simply summing the virial mass of its member clusters. The virial masses of the clusters in our sample were estimated using the  $M_{500}$  obtained from the Lovisari et al. (2015)  $L - M$  scaling relation (see Sect. 5). We then converted  $M_{500}$  to  $M_{\text{vir}}$  by assuming an NFW profile (Navarro et al. 1997) with concentration  $c \equiv r_{200}/r_s = 4$ , which approximately gives  $M_{\text{vir}} \approx 2M_{500}$  (Reiprich et al. 2013).

We also adopted a new parameter: compactness,  $C$ , to describe the spatial distribution of member clusters within the supercluster.  $C$  is defined in the following way. We consider a sphere whose diameter is equal to the linking length, the position of this sphere is adjusted until the total mass of the member clusters enclosed reaches its maximum value.  $C$  is then defined as the ratio of the maximum enclosed mass and the total mass of the supercluster. Therefore, if all the member clusters are distributed within the linking length, the compactness will be 1.

Clearly,  $C$  is very sensitive to the reliability of the distance between member clusters, thus is affected by the uncertainties in photometric redshift measurements. The precision of  $C$  is also dependent on the multiplicity of a supercluster. Among the 19 superclusters candidates, we measure a compactness  $C = 1$  for six. Most of them have compactness larger than 0.5. Limited by the sample size and the narrow redshift span (most of the supercluster candidates are below  $z = 0.5$ ), we are not able to make further analysis on compactness. On the other hand, an increasing of supercluster compactness from high- $z$  to low- $z$  can be anticipated, and can be investigated in future works, provided that a larger and more complete supercluster sample is available, especially in high redshifts.

With the 3D distribution of member clusters and their total mass, we further explore the collapsing probability for each supercluster candidate. Assuming  $\Lambda$ CDM cosmology, an object with overdensity  $\delta_c \equiv \rho/\rho_c$  higher than  $\sim 1.7$  will finally collapse. Clearly, since superclusters do not have regular shapes, their volume cannot be measured directly. Moreover, we only know the mass in the most massive member clusters that are detectable, while the fraction of mass in filaments and low-mass subhalos is unavailable. Therefore, the density within a supercluster cannot be accurately measured. Nevertheless, we can obtain a very conservative lower limit of the density by dividing the total virial masses of the member clusters by the volume of the smallest sphere which encloses all the member clusters. Interestingly, with this very conservative estimation, we still found two superclusters: eFEDS-SC12 and eFEDS-SC13, with  $\delta_c = 2.2$  and  $6.1$ , implying that they will finally collapse with a high probability. The radii of the smallest sphere are  $11.8$  Mpc and  $7.3$  Mpc, respectively. This is consistent with their compactness: both the two superclusters have compactness equal to 1. From Table B.1 and Fig. B.1, it is also notable that the cluster members of these two superclusters distribute very close to each other. On the other hand, we are not able to constrain the collapsing time of the two superclusters, which obviously should take into account not only gravity, but also the effect of dark energy, and the 3D distribution of mass within the supercluster. We therefore defer this study to a future work.

In this work we also confirm the detection of the supercluster discovered by [Ghirardini et al. \(2021\)](#). However, this supercluster is found fragmented into two parts, eFEDS-SC11 and eFEDS-SC12, each with 4 members. This is due to the change in the redshifts of the member clusters. [Ghirardini et al. \(2021\)](#) adopted the photometric redshifts from HSC survey data available at the time of submission, while here in this work we use the latest spectroscopic redshifts (see Sect. 2.3). This difference also highlights the importance of using the most accurate spectroscopic redshifts in the search for superclusters. We also note that, although the supercluster discovered in [Ghirardini et al. \(2021\)](#) is fragmented into eFEDS-SC11 and eFEDS-SC12 in this work, they are still very close to each other, with the closest members of eFEDS-SC11 and eFEDS-SC12 separated by  $\sim 29$  Mpc, only slightly exceeding the linking length at their redshift,  $\sim 28$  Mpc. This  $\sim 1$  Mpc difference is within the virial radius of a cluster, thus eFEDS-SC11 and eFEDS-SC12 probably belong to the same structure. We therefore confirm that our results are fully consistent with [Ghirardini et al. \(2021\)](#).

Most of the supercluster candidates are located in the redshift range [0.1–0.5], with four high- $z$  candidates beyond redshift 0.5: eFEDS-SC16 at 0.565, eFEDS-SC17 at 0.579, eFEDS-SC18 at 0.619, and eFEDS-SC19 at 0.803. However, we note that we only have photometric redshifts for most members of these superclusters (see Table B.1). Moreover, the linking length

increases rapidly to  $>50$  Mpc at high redshifts due to the low number density of high-redshift clusters in our catalog. Considering the relatively large uncertainty in the photometric redshift and the low statistic at high- $z$ , we note that these candidates need to be verified by future spectroscopic follow-up observations.

## 7. Conclusions

In this paper, we present the first catalog of eROSITA selected galaxy cluster and group candidates and their physical properties, detected in the sky area covered by the eROSITA Final Equatorial-Depth Survey (eFEDS). The optical follow-up for redshift and confirmation is performed using the MCMF tool on basis of data from the HSC-SSP survey and the DECaLS survey. Our conclusions are summarized below.

In the 140 square degree area covered by eFEDS, we detected 542 candidate clusters and groups of galaxies, down to the flux limit of  $\sim 10^{-14}$  erg s $^{-1}$  cm $^{-2}$  in the soft band (0.5–2 keV) within 1'. The clusters are distributed in the redshift range  $z = [0.01, 1.3]$ , with the median redshift  $z_{\text{median}} = 0.35$ . The contamination fraction of non-cluster sources in the sample, dominated by AGN misidentified as extended sources, is  $\sim 1/5$ , obtained from simulations. After accounting for the contamination, we find a cluster density of  $\sim 3.2$  per square degree at this depth, in agreement with the expectations in [Merloni et al. \(2012\)](#). Our simulations suggest that it is possible to obtain a sample with a purity of  $>90\%$  if a simple cut at  $\mathcal{L}_{\text{ext}} > 15$  is applied. This further selection delivers a subsample of  $\sim 270$  clusters. However we note that the sample volume is unavoidably reduced as the high-redshift tail of the sample will have a smaller extent, and therefore be more severely cut by a higher  $\mathcal{L}_{\text{ext}}$  threshold. Most of these high-redshift clusters, however, are real, and the simulations predict that a few more of them will be found among the point-source detected population. In a following paper (Bulbul et al., in prep.), we will present a detailed assessment of the contribution of unresolved clusters to the eFEDS point-sources catalog. Further improvement on the characterization of the high-redshift clusters will be obtained thanks to the recently completed SDSS-IV and SDSS-V spectroscopic follow-up campaign, that will be presented elsewhere (Ider-Chitham et al., in prep.). We also found that  $\sim 16\%$  of the clusters can be matched with a counterpart in the published X-ray or SZ cluster catalogs, indicating that the majority of the clusters in the sample are detected through their ICM emission for the first time.

We measure the ICM temperature within two parametric radii, 300 kpc and 500 kpc. Radial profiles of flux, luminosity, electron density, and gas mass are measured from the soft band surface brightness image. For  $\sim 1/5$  of the clusters in the sample (102/542), we obtain  $> 2\sigma$  constraints on temperature. The average temperature of these clusters is  $\sim 2$  keV. The clusters span the luminosity range [ $10^{41}$  erg s $^{-1}$ ,  $\sim 10^{44}$  erg s $^{-1}$ ]. According to the  $L - M$  scaling relation in [Lovisari et al. \(2015\)](#),  $\sim 40\%$  of the clusters have  $M_{500} < 10^{14} M_{\odot}$ , indicating that our sample is dominated by galaxy groups and low-mass clusters, as expected.

The selection function, the purity and completeness of the catalog are examined and discussed in detail using the state-of-the-art simulations of the eFEDS field. The X-ray Luminosity Function of the sample is found to agree well with the results obtained from other recent X-ray surveys, such as the XXL and the WARPS surveys. We find no significant evolution of the cluster XLF in the redshift range [0.01, 1.3].

Using the redshifts and spatial distribution of the clusters, we performed a search for superclusters in the eFEDS field, and detected 19 supercluster candidates, most of which are located

at redshifts between 0.1 and 0.5, including the one at  $z \sim 0.36$  already published in [Ghirardini et al. \(2021\)](#). Another four high- $z$  supercluster candidates are detected at redshifts higher than 0.5, but need further spectroscopic confirmation as the errors on the photometric redshifts may bias the linking length calculations.

The eFEDS cluster and group catalog at the final eRASS equatorial depth provides a benchmark proof-of-concept for the eROSITA All-Sky Survey extended source detection and characterization. We confirm the excellent performance of eROSITA for cluster science and expect no significant deviations from our pre-launch expectations for the final All-Sky Survey.

**Acknowledgements.** This work is based on data from eROSITA, the soft X-ray instrument aboard SRG, a joint Russian-German science mission supported by the Russian Space Agency (Roskosmos), in the interests of the Russian Academy of Sciences represented by its Space Research Institute (IKI), and the Deutsches Zentrum für Luft- und Raumfahrt (DLR). The SRG spacecraft was built by Lavochkin Association (NPOL) and its subcontractors, and is operated by NPOL with support from the Max Planck Institute for Extraterrestrial Physics (MPE). The development and construction of the eROSITA X-ray instrument was led by MPE, with contributions from the Dr. Karl Remeis Observatory Bamberg & ECAP (FAU Erlangen-Nürnberg), the University of Hamburg Observatory, the Leibniz Institute for Astrophysics Potsdam (AIP), and the Institute for Astronomy and Astrophysics of the University of Tübingen, with the support of DLR and the Max Planck Society. The Argelander Institute for Astronomy of the University of Bonn and the Ludwig-Maximilians-Universität München also participated in the science preparation for eROSITA.

The eROSITA data shown here were processed using the eSASS/NRTA software system developed by the German eROSITA consortium.

The Hyper Suprime-Cam (HSC) collaboration includes the astronomical communities of Japan and Taiwan, and Princeton University. The HSC instrumentation and software were developed by the National Astronomical Observatory of Japan (NAOJ), the Kavli Institute for the Physics and Mathematics of the Universe (Kavli IPMU), the University of Tokyo, the High Energy Accelerator Research Organization (KEK), the Academia Sinica Institute for Astronomy and Astrophysics in Taiwan (ASIAA), and Princeton University. Funding was contributed by the FIRST program from the Japanese Cabinet Office, the Ministry of Education, Culture, Sports, Science and Technology (MEXT), the Japan Society for the Promotion of Science (JSPS), Japan Science and Technology Agency (JST), the Toray Science Foundation, NAOJ, Kavli IPMU, KEK, ASIAA, and Princeton University.

This paper makes use of software developed for the Large Synoptic Survey Telescope. We thank the LSST Project for making their code available as free software at <http://dm.lsst.org>.

This paper is based [in part] on data collected at the Subaru Telescope and retrieved from the HSC data archive system, which is operated by Subaru Telescope and Astronomy Data Center (ADC) at NAOJ. Data analysis was in part carried out with the cooperation of Center for Computational Astrophysics (CfCA), NAOJ.

This work was supported in part by World Premier International Research Center Initiative (WPI Initiative), MEXT, Japan, and JSPS KAKENHI Grant Number JP19KK0076.

This work was supported in part by CNES.

This work was supported in part by the Fund for the Promotion of Joint International Research, JSPS KAKENHI Grant Number 16KK0101.

DNH acknowledges support from the ERC through the grant ERC-Stg DRA-NOEL n. 714245.

E.B. acknowledges financial support from the European Research Council (ERC) Consolidator Grant under the European Union's Horizon 2020 research and innovation programme (grant agreement No 101002585).

- Arnaud, M., Pratt, G. W., Piffaretti, R., et al. 2010, *A&A*, 517, A92  
 Asplund, M., Grevesse, N., Sauval, A. J., & Scott, P. 2009, *ARA&A*, 47, 481  
 Barber, C. B., Dobkin, D. P., & Huhdanpaa, H. 1996, *ACM Trans. Math. Softw.*, 22, 469–483  
 Blanton, M. R., Bershadsky, M. A., Abolfathi, B., et al. 2017, *AJ*, 154, 28  
 Bleem, L. E., Stalder, B., de Haan, T., et al. 2015, *ApJS*, 216, 27  
 Böhringer, H., Chon, G., & Collins, C. A. 2014, *A&A*, 570, A31  
 Böhringer, H., Chon, G., Retzlaff, J., et al. 2017, *AJ*, 153, 220  
 Böhringer, H., Schuecker, P., Guzzo, L., et al. 2001, *A&A*, 369, 826  
 Böhringer, H., Schuecker, P., Pratt, G. W., et al. 2007, *A&A*, 469, 363  
 Böhringer, H., Voges, W., Huchra, J. P., et al. 2000, *ApJS*, 129, 435  
 Borm, K., Reiprich, T. H., Mohammed, I., & Lovisari, L. 2014, *A&A*, 567, A65  
 Bosch, J., Armstrong, R., Bickerton, S., et al. 2018, *PASJ*, 70, S5  
 Breiman, L. 2001, *Machine Learning*, 45, 5  
 Bulbul, E., Chiu, I. N., Mohr, J. J., et al. 2019, *ApJ*, 871, 50  
 Bulbul, G. E., Hasler, N., Bonamente, M., & Joy, M. 2010, *ApJ*, 720, 1038  
 Bulbul, G. E., Smith, R. K., Foster, A., et al. 2012, *ApJ*, 747, 32  
 Cappelluti, N., Hasinger, G., Brusa, M., et al. 2007, *ApJS*, 172, 341  
 Cash, W. 1979, *ApJ*, 228, 939  
 Chon, G., Böhringer, H., & Nowak, N. 2013, *MNRAS*, 429, 3272  
 Chow-Martínez, M., Andernach, H., Caretta, C. A., & Trejo-Alonso, J. J. 2014, *MNRAS*, 445, 4073  
 Chuang, C.-H., Yepes, G., Kitaura, F.-S., et al. 2019, *MNRAS*, 487, 48  
 Clerc, N., Ramos-Ceja, M. E., Ridl, J., et al. 2018, *A&A*, 617, A92  
 Clerc, N., Sadibekova, T., Pierre, M., et al. 2012, *MNRAS*, 423, 3561  
 Comparat, J., Eckert, D., Finoguenov, A., et al. 2020, *The Open Journal of Astrophysics*, 3, 13  
 Comparat, J., Merloni, A., Salvato, M., et al. 2019, *MNRAS*, 487, 2005  
 Coupon, J., Czakon, N., Bosch, J., et al. 2018, *PASJ*, 70, S7  
 Dauser, T., Falkner, S., Lorenz, M., et al. 2019, *A&A*, 630, A66  
 De Grandi, S., Böhringer, H., Guzzo, L., et al. 1999, *ApJ*, 514, 148  
 Dennerl, K., Andritschke, R., Bräuninger, H., et al. 2020, in *Society of Photo-Optical Instrumentation Engineers (SPIE) Conference Series*, Vol. 11444, *Society of Photo-Optical Instrumentation Engineers (SPIE) Conference Series*, 114444Q  
 Dey, A., Schlegel, D. J., Lang, D., et al. 2019, *AJ*, 157, 168  
 Driver, S. P., Norberg, P., Baldry, I. K., et al. 2009, *Astronomy and Geophysics*, 50, 5.12  
 Ebeling, H., Edge, A. C., Böhringer, H., et al. 1998, *MNRAS*, 301, 881  
 Ebeling, H., Edge, A. C., & Henry, J. P. 2001, *ApJ*, 553, 668  
 Ebeling, H., Mullis, C. R., & Tully, R. B. 2002, *ApJ*, 580, 774  
 Eckmiller, H. J., Hudson, D. S., & Reiprich, T. H. 2011, *A&A*, 535, A105  
 Einasto, M., Einasto, J., Tago, E., Dalton, G. B., & Andernach, H. 1994, *MNRAS*, 269, 301  
 Einasto, M., Einasto, J., Tago, E., Müller, V., & Andernach, H. 2001, *AJ*, 122, 2222  
 Ettori, S., Ghirardini, V., Eckert, D., et al. 2019, *A&A*, 621, A39  
 Finoguenov, A., Guzzo, L., Hasinger, G., et al. 2007, *ApJS*, 172, 182  
 Finoguenov, A., Rykoff, E., Clerc, N., et al. 2020, *A&A*, 638, A114  
 Finoguenov, A., Tanaka, M., Cooper, M., et al. 2015, *A&A*, 576, A130  
 Finoguenov, A., Watson, M. G., Tanaka, M., et al. 2010, *MNRAS*, 403, 2063  
 Foreman-Mackey, D., Hogg, D. W., Lang, D., & Goodman, J. 2013, *PASP*, 125, 306  
 Foster, A. R., Ji, L., Smith, R. K., & Brickhouse, N. S. 2012, *ApJ*, 756, 128  
 Freyberg, M., Perinati, E., Pacaud, F., et al. 2020, in *Society of Photo-Optical Instrumentation Engineers (SPIE) Conference Series*, Vol. 11444, *Society of Photo-Optical Instrumentation Engineers (SPIE) Conference Series*, 114441O  
 Furusawa, H., Koike, M., Takata, T., et al. 2018, *PASJ*, 70, S3  
 Ghirardini, V., Bulbul, E., Hoang, D. N., et al. 2021, *A&A*, 647, A4  
 Giodini, S., Lovisari, L., Pointecouteau, E., et al. 2013, *Space Sci. Rev.*, 177, 247  
 Gozaliasl, G., Finoguenov, A., Tanaka, M., et al. 2019, *MNRAS*, 483, 3545  
 Hasinger, G., Cappelluti, N., Brunner, H., et al. 2007, *ApJS*, 172, 29  
 Hasselfield, M., Hilton, M., Marriage, T. A., et al. 2013, *J. Cosmology Astropart. Phys.*, 2013, 008  
 Hensman, J., Matthews, A., & Ghahramani, Z. 2015, in *Proceedings of the Eighteenth International Conference on Artificial Intelligence and Statistics*, ed. G. Guy Lebanon & S. V. N. Vishwanathan, Vol. 38, 351–360  
 Hilton, M., Sifón, C., Naess, S., et al. 2021, *ApJS*, 253, 3  
 Huang, S., Leauthaud, A., Murata, R., et al. 2018, *PASJ*, 70, S6  
 Huchra, J. P., Macri, L. M., Masters, K. L., et al. 2012, *ApJS*, 199, 26  
 Kawanomoto, S., Uraguchi, F., Komiyama, Y., et al. 2018, *PASJ*, 70, 66  
 Klein, M., Grandis, S., Mohr, J. J., et al. 2019, *MNRAS*, 488, 739  
 Klein, M., Mohr, J. J., Desai, S., et al. 2018, *MNRAS*, 474, 3324  
 Koens, L. A., Maughan, B. J., Jones, L. R., et al. 2013, *MNRAS*, 435, 3231  
 Komiyama, Y., Chiba, M., Tanaka, M., et al. 2018, *ApJ*, 853, 29  
 Koulouridis, E., Clerc, N., Sadibekova, T., et al. 2021, *arXiv e-prints*, arXiv:2104.06617  
 Kuntz, K. D. & Snowden, S. L. 2000, *ApJ*, 543, 195  
 Liu, A., Tozzi, P., Ettori, S., et al. 2020, *A&A*, 637, A58

## References

- Adami, C., Giles, P., Koulouridis, E., et al. 2018, *A&A*, 620, A5  
 Aihara, H., AlSayyad, Y., Ando, M., et al. 2019, *arXiv:1905.12221*, arXiv:1905.12221  
 Aihara, H., Arimoto, N., Armstrong, R., et al. 2018a, *PASJ*, 70, S4  
 Aihara, H., Armstrong, R., Bickerton, S., et al. 2018b, *PASJ*, 70, S8  
 Allen, S. W., Evrard, A. E., & Mantz, A. B. 2011, *ARA&A*, 49, 409  
 Allen, S. W., Schmidt, R. W., Fabian, A. C., & Ebeling, H. 2003, *MNRAS*, 342, 287  
 Andrade-Santos, F., Pratt, G. W., Melin, J.-B., et al. 2021, *arXiv e-prints*, arXiv:2103.07545  
 Arnaud, K. A. 1996, in *Astronomical Society of the Pacific Conference Series*, Vol. 101, *Astronomical Data Analysis Software and Systems V*, ed. G. H. Jacoby & J. Barnes, 17

- Liu, A., Yu, H., Tozzi, P., & Zhu, Z.-H. 2015, ApJ, 809, 27
- Lovisari, L., Reiprich, T. H., & Schellenberger, G. 2015, A&A, 573, A118
- Luo, B., Brandt, W. N., Xue, Y. Q., et al. 2017, ApJS, 228, 2
- Merloni, A., Predehl, P., Becker, W., et al. 2012, arXiv e-prints, arXiv:1209.3114
- Miyazaki, S., Komiyama, Y., Kawanomoto, S., et al. 2018, PASJ, 70, S1
- Mullis, C. R., Vikhlinin, A., Henry, J. P., et al. 2004, ApJ, 607, 175
- Navarro, J. F., Frenk, C. S., & White, S. D. M. 1997, ApJ, 490, 493
- Nishizawa, A. J., Hsieh, B.-C., Tanaka, M., & Takata, T. 2020, arXiv e-prints, arXiv:2003.01511
- Oguri, M., Lin, Y.-T., Lin, S.-C., et al. 2018, PASJ, 70, S20
- Okabe, N., Dicker, S., Eckert, D., et al. 2021, MNRAS, 501, 1701
- Pacaud, F., Clerc, N., Giles, P. A., et al. 2016, A&A, 592, A2
- Pacaud, F., Pierre, M., Melin, J. B., et al. 2018, A&A, 620, A10
- Pedregosa, F., Varoquaux, G., Gramfort, A., et al. 2011, Journal of Machine Learning Research, 12, 2825
- Pierre, M., Chiappetti, L., Pacaud, F., et al. 2007, MNRAS, 382, 279
- Pierre, M., Pacaud, F., Adam, C., et al. 2016, A&A, 592, A1
- Piffaretti, R., Arnaud, M., Pratt, G. W., Pointecouteau, E., & Melin, J.-B. 2011, A&A, 534, A109
- Pillepich, A., Porciani, C., & Reiprich, T. H. 2012, MNRAS, 422, 44
- Planck Collaboration, Ade, P. A. R., Aghanim, N., et al. 2016a, A&A, 594, A27
- Planck Collaboration, Ade, P. A. R., Aghanim, N., et al. 2016b, A&A, 594, A13
- Planck Collab., Ade, P. A. R., Aghanim, N., et al. 2014, A&A, 571, A29
- Pratt, G. W., Arnaud, M., Biviano, A., et al. 2019, Space Sci. Rev., 215, 25
- Pratt, G. W., Croston, J. H., Arnaud, M., & Böhringer, H. 2009, A&A, 498, 361
- Predehl, P., Andritschke, R., Arefiev, V., et al. 2021, A&A, 647, A1
- Rasmussen, C. E. & Williams, C. K. I. 2006, Gaussian processes for machine learning (MIT Press)
- Reiprich, T. H., Basu, K., Ettori, S., et al. 2013, Space Sci. Rev., 177, 195
- Ridl, J., Clerc, N., Sadibekova, T., et al. 2017, MNRAS, 468, 662
- Rosati, P., Borgani, S., & Norman, C. 2002, ARA&A, 40, 539
- Rosati, P., Della Ceca, R., Norman, C., & Giacconi, R. 1998, ApJ, 492, L21
- Rykoff, E. S., Rozo, E., Hollowood, D., et al. 2016, ApJS, 224, 1
- Salvato, M., Buchner, J., Budavári, T., et al. 2018, MNRAS, 473, 4937
- Sanders, J. S., Dennerl, K., Russell, H. R., et al. 2020, A&A, 633, A42
- Sanders, J. S. & Fabian, A. C. 2006, MNRAS, 370, 63
- Seppi, R., Comparat, J., Nandra, K., et al. 2020, arXiv e-prints, arXiv:2008.03179
- Sereno, M., Umetsu, K., Ettori, S., et al. 2020, MNRAS, 492, 4528
- Smith, R. K., Brickhouse, N. S., Liedahl, D. A., & Raymond, J. C. 2001, ApJ, 556, L91
- Snowden, S. L., Mushotzky, R. F., Kuntz, K. D., & Davis, D. S. 2008, A&A, 478, 615
- Tanaka, M. 2015, ApJ, 801, 20
- Umetsu, K. 2020, A&A Rev., 28, 7
- Vikhlinin, A., Burenin, R. A., Ebeling, H., et al. 2009, ApJ, 692, 1033
- Vikhlinin, A., Kravtsov, A., Forman, W., et al. 2006, ApJ, 640, 691
- Vikhlinin, A., McNamara, B. R., Forman, W., et al. 1998, ApJ, 498, L21
- Voges, W., Aschenbach, B., Boller, T., et al. 1999, A&A, 349, 389
- Wager, S., Hastie, T., & Efron, B. 2014, Journal of Machine Learning Research, 15, 1625
- Wen, Z. L., Han, J. L., & Liu, F. S. 2012, ApJS, 199, 34
- Willingale, R., Starling, R. L. C., Beardmore, A. P., Tanvir, N. R., & O'Brien, P. T. 2013, MNRAS, 431, 394
- Wilms, J., Allen, A., & McCray, R. 2000, ApJ, 542, 914
- Zucca, E., Zamorani, G., Scaramella, R., & Vettolani, G. 1993, ApJ, 407, 470

<sup>1</sup>Max Planck Institute for Extraterrestrial Physics, Giessenbachstrasse

1, 85748 Garching, Germany

<sup>2</sup>Universitaets-Sternwarte Muenchen, Fakultaet fuer Physik, LMU

Munich, Scheinerstr. 1, 81679 Munich, Germany

<sup>3</sup>IRAP, Université de Toulouse, CNRS, UPS, CNES, Toulouse, France<sup>4</sup>Argelander-Institut für Astronomie (AIfA), Universität Bonn, Auf dem Hügel 71, 53121 Bonn, Germany<sup>5</sup>Physics Program, Graduate School of Advanced Science and Engineering, Hiroshima University, 1-3-1 Kagamiyama, Higashi-Hiroshima, Hiroshima 739-8526, Japan<sup>6</sup>Hiroshima Astrophysical Science Center, Hiroshima University, 1-3-1 Kagamiyama, Higashi-Hiroshima, Hiroshima 739-8526, Japan<sup>7</sup>Core Research for Energetic Universe, Hiroshima University, 1-3-1, Kagamiyama, Higashi-Hiroshima, Hiroshima 739-8526, Japan<sup>8</sup>INAF - Osservatorio Astronomico di Trieste, via Tiepolo 11, I-34143

Trieste, Italy

<sup>9</sup>IFPU - Institute for Fundamental Physics of the Universe, Via Beirut

2, I-34014 Trieste, Italy

<sup>10</sup>University of Hamburg, Hamburger Sternwarte, Gojenbergsweg 112,

Article number, page 18 of 24

## Appendix A: Properties of supercluster candidates

We list in Table B.1 the member clusters of the supercluster candidates detected in the eFEDS field, as described in Sect. 6. In Fig. B.1 we show the X-ray images of these superclusters. The galaxy density maps from the HSC-SSP survey data at the corresponding redshifts for all the superclusters are shown in Fig. B.2.

## Appendix B: Main results of X-ray analysis

In this section we list the main results of the X-ray analysis. Particularly, instead of providing the results for all the 542 clusters, we selected a subsample of 102 clusters with  $> 2\sigma$  temperature measurements within either 300 kpc or 500 kpc. The results of the clusters in the subsample are listed in Table B.2.

**Table B.1.** The member clusters of the 19 superclusters in the eFEDS field.

SC ID	Cluster ID	RA [deg]	Dec [deg]	$z$	type	$M_{500}$ $[10^{14} M_\odot]$
eFEDS-SC1	eFEDS J085706.0+011453	134.2749	+1.2482	0.106	1	0.4
	eFEDS J085433.0+004009	133.6376	+0.6693	0.109	1	0.1
	eFEDS J085142.0+021438	132.9248	+2.2440	0.107	1	0.1
	eFEDS J085436.6+003835	133.6526	+0.6431	0.106	1	1.2
eFEDS-SC2	eFEDS J085327.2-002117	133.3634	-0.3549	0.193	1	0.6
	eFEDS J085340.6+022411	133.4191	+2.4032	0.196	1	0.6
	eFEDS J085022.3+001607	132.5927	+0.2687	0.196	1	1.0
	eFEDS J085027.9+001503	132.6160	+0.2509	0.197	1	2.6
eFEDS-SC3	eFEDS J085030.5+003330	132.6272	+0.5584	0.192	1	1.1
	eFEDS J085128.5+011502	132.8685	+1.2505	0.197	1	0.1
	eFEDS J085751.7+031039	134.4653	+3.1775	0.201	1	5.7
	eFEDS J090137.7+030254	135.4072	+3.0483	0.188	0	0.2
eFEDS-SC4	eFEDS J090200.6+022339	135.5024	+2.3943	0.202	1	1.0
	eFEDS J085913.1+031335	134.8048	+3.2263	0.189	1	0.9
	eFEDS J085931.9+030839	134.8830	+3.1443	0.196	1	2.2
	eFEDS J090255.2+030220	135.7300	+3.0389	0.200	1	1.0
eFEDS-SC5	eFEDS J090010.4+023631	135.0435	+2.6086	0.200	1	0.4
	eFEDS J090119.0+030204	135.3294	+3.0345	0.193	1	0.5
	eFEDS J085728.3+032354	134.3680	+3.3984	0.200	1	0.6
	eFEDS J090131.2+030056	135.3800	+3.0157	0.193	1	3.1
eFEDS-SC6	eFEDS J092209.4+034628	140.5391	+3.7746	0.270	1	3.8
	eFEDS J092220.4+034806	140.5852	+3.8017	0.267	1	1.0
	eFEDS J092246.2+034251	140.6928	+3.7143	0.269	1	1.2
	eFEDS J092302.6+034002	140.7611	+3.6673	0.269	0	0.8
eFEDS-SC7	eFEDS J092022.8+045013	140.0954	+4.8369	0.270	1	1.4
	eFEDS J083916.8-020552	129.8198	-2.0979	0.269	0	0.6
	eFEDS J083918.0-020839	129.8247	-2.1442	0.269	0	0.5
	eFEDS J083921.1-014149	129.8377	-1.6970	0.269	1	1.2
eFEDS-SC8	eFEDS J083930.4-014348	129.8763	-1.7302	0.271	0	0.6
	eFEDS J083933.9-014044	129.8909	-1.6790	0.272	1	4.9
	eFEDS J084000.1-013110	130.0002	-1.5194	0.266	1	1.2
	eFEDS J084152.0-010156	130.4665	-1.0323	0.270	1	0.4
eFEDS-SC9	eFEDS J092053.5+021126	140.2228	+2.1905	0.280	1	0.6
	eFEDS J092049.5+024513	140.2063	+2.7538	0.284	1	4.1
	eFEDS J092031.3+024711	140.1306	+2.7863	0.278	1	0.4
	eFEDS J091849.0+021205	139.7042	+2.2013	0.283	1	3.3
eFEDS-SC10	eFEDS J090141.0-012132	135.4207	-1.3591	0.295	1	1.1
	eFEDS J090146.3-013756	135.4427	-1.6322	0.295	1	1.5
	eFEDS J090154.0-012209	135.4748	-1.3694	0.295	1	1.3
	eFEDS J090053.1-002837	135.2212	-0.4772	0.295	1	0.6
eFEDS-SC11	eFEDS J085121.2+012857	132.8384	+1.4825	0.327	1	0.8
	eFEDS J085517.3+013508	133.8219	+1.5857	0.324	1	2.0
	eFEDS J084935.0+014437	132.3958	+1.7438	0.325	1	1.4
	eFEDS J085624.4+004632	134.1016	+0.7757	0.319	1	0.8
eFEDS-SC12	eFEDS J092846.6+000056	142.1940	+0.0157	0.344	1	1.4
	eFEDS J092549.0-011725	141.4539	-1.2903	0.337	0	1.5
	eFEDS J092621.4-003356	141.5890	-0.5657	0.340	0	0.9
	eFEDS J092739.8-010427	141.9158	-1.0743	0.329	1	1.8

**Table B.1.** continued.

SC ID	Cluster ID	RA [deg]	Dec [deg]	$z$	type	$M_{500}$ $[10^{14} M_\odot]$
eFEDS-SC10	eFEDS J092740.8-015320	141.9196	-1.8889	0.332	1	1.0
	eFEDS J092405.1-013059	141.0211	-1.5165	0.337	1	2.4
	eFEDS J084253.7+002006	130.7238	+0.3350	0.345	0	0.5
	eFEDS J084418.0+010416	131.0748	+1.0711	0.340	1	2.3
	eFEDS J084004.9+013751	130.0203	+1.6309	0.342	0	0.6
eFEDS-SC11	eFEDS J084346.2+010833	130.9425	+1.1425	0.342	1	0.8
	eFEDS J093544.2-000339	143.9342	-0.0609	0.347	1	1.6
	eFEDS J093316.7+004619	143.3195	+0.7721	0.347	0	0.3
	eFEDS J093546.4-000115	143.9433	-0.0211	0.339	1	2.1
eFEDS-SC12	eFEDS J093431.3-002309	143.6304	-0.3860	0.342	1	2.6
	eFEDS J093612.7+001650	144.0529	+0.2807	0.358	1	1.9
	eFEDS J093500.8+005417	143.7532	+0.9048	0.361	1	3.3
	eFEDS J093513.1+004757	143.8046	+0.7994	0.356	1	7.9
eFEDS-SC13	eFEDS J093520.7+003448	143.8363	+0.5802	0.355	1	1.7
	eFEDS J083900.6+020057	129.7527	+2.0159	0.359	1	2.6
	eFEDS J083803.0+015626	129.5124	+1.9407	0.360	1	2.0
	eFEDS J083857.6+020847	129.7398	+2.1464	0.360	1	4.0
eFEDS-SC14	eFEDS J083859.3+022841	129.7473	+2.4782	0.359	1	1.4
	eFEDS J084110.9+005200	130.2953	+0.8668	0.415	0	0.8
	eFEDS J084124.7+004636	130.3530	+0.7768	0.407	1	1.2
	eFEDS J084129.0+002645	130.3708	+0.4460	0.402	1	2.3
eFEDS-SC15	eFEDS J084501.0+012728	131.2542	+1.4578	0.420	1	2.6
	eFEDS J084210.5+020559	130.5439	+2.0997	0.421	0	0.4
	eFEDS J084221.0+013844	130.5875	+1.6457	0.421	1	3.4
	eFEDS J084649.1+004946	131.7045	+0.8295	0.416	1	0.7
eFEDS-SC16	eFEDS J084051.7+014122	130.2156	+1.6895	0.411	1	1.7
	eFEDS J091302.1+035001	138.2590	+3.8336	0.455	0	2.7
	eFEDS J091305.9+035022	138.2747	+3.8394	0.456	1	2.7
	eFEDS J091315.0+034850	138.3125	+3.8139	0.453	1	4.9
eFEDS-SC17	eFEDS J091522.5+041201	138.8438	+4.2003	0.460	1	1.0
	eFEDS J083427.1-015613	128.6129	-1.9369	0.573	0	1.5
	eFEDS J083927.1-021358	129.8627	-2.2328	0.567	0	1.3
	eFEDS J083929.7-015005	129.8736	-1.8348	0.575	0	2.1
eFEDS-SC18	eFEDS J083809.5-020450	129.5394	-2.0808	0.550	0	1.4
	eFEDS J083812.0-015934	129.5496	-1.9930	0.560	0	10.3
	eFEDS J083817.6-021704	129.5732	-2.2845	0.565	0	5.4
	eFEDS J092041.2+041118	140.1716	+4.1883	0.580	0	1.4
eFEDS-SC19	eFEDS J091757.1+050915	139.4881	+5.1542	0.586	0	7.3
	eFEDS J092258.2+032041	140.7426	+3.3449	0.575	0	1.9
	eFEDS J092031.9+040621	140.1329	+4.1059	0.575	1	2.2
	eFEDS J090752.0+024647	136.9666	+2.7797	0.618	1	2.0
eFEDS-SC19	eFEDS J090336.8+033125	135.9033	+3.5235	0.617	0	1.7
	eFEDS J091254.5+032029	138.2270	+3.3414	0.619	0	4.6
	eFEDS J091648.2+030506	139.2007	+3.0851	0.620	1	2.4
	eFEDS J090637.0+010852	136.6542	+1.1479	0.786	0	3.5
eFEDS-SC19	eFEDS J090700.8+011032	136.7531	+1.1757	0.799	0	2.0
	eFEDS J090033.8+033933	135.1408	+3.6591	0.809	0	3.3
	eFEDS J090757.6+025428	136.9900	+2.9077	0.798	1	3.6
	eFEDS J090418.7+020642	136.0778	+2.1117	0.808	0	4.3
eFEDS-SC19	eFEDS J090452.5+033326	136.2187	+3.5574	0.808	0	5.7
	eFEDS J090821.9+025141	137.0913	+2.8615	0.812	0	3.4

**Notes.** Redshift type: 0 for photometric redshift and 1 for spectroscopic redshift.  $M_{500}$  in the last column is estimated using the scaling relation in Lovisari et al. (2015).

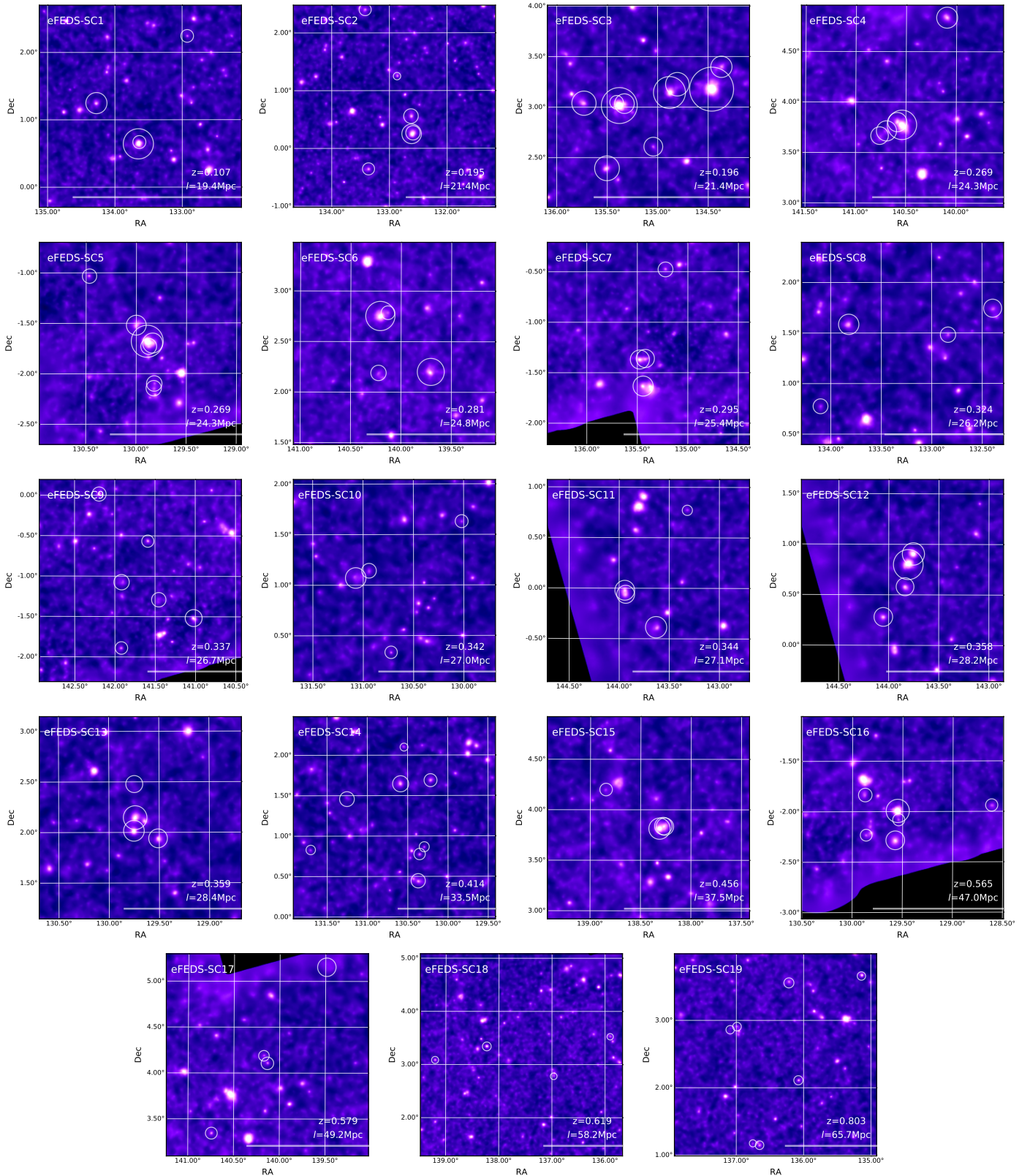


**Fig. B.1.** X-ray images of the 19 superclusters we detected in the eFEDS field. The images are generated in the same way as for Fig. 1. The white circles mark the estimated virial radii of the member clusters of each supercluster. The thick bar in the lower right corner indicates the linking length at the supercluster's redshift.

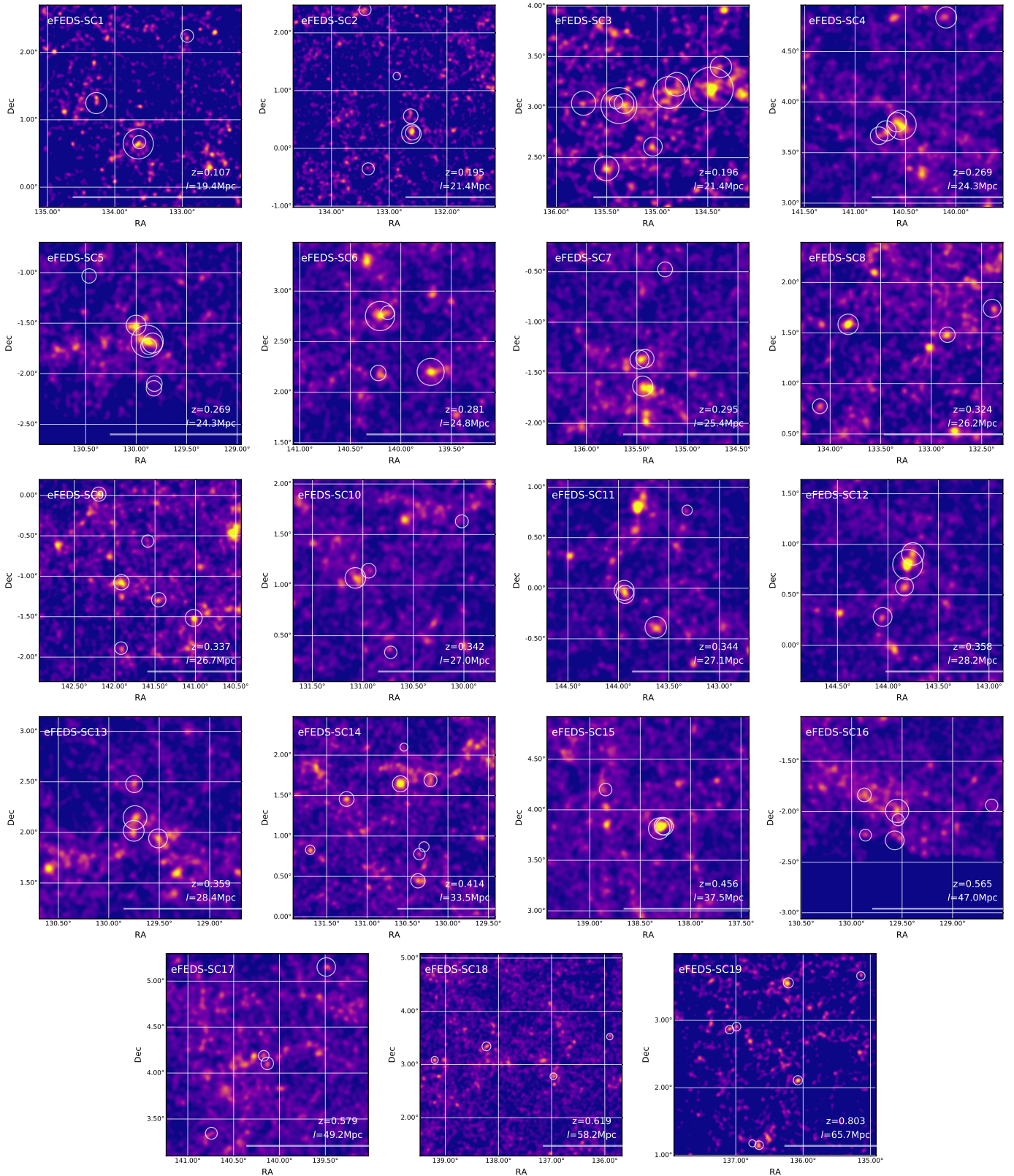


**Fig. B.2.** Galaxy density map from HSC-SSP survey data at the locations and redshifts of the 19 supercluster candidates. They are obtained by integrating the full probability function of the MIZUKI (Tanaka 2015) photometric redshifts ( $P(z)$ ) of each galaxy (the S19A catalog; Nishizawa et al. 2020) with a width of the redshift slice of  $\Delta z = 0.05$ ;  $\int_{z-\Delta z}^{z+\Delta z} P(z)dz / \int_0^{\infty} P(z)dz$ , in a similar way of Okabe et al. (2021). The galaxies are brighter than 23 ABmag. The smoothing scale is FWHM= 3 arcmin.

**Table B.2.** Main results of the X-ray analysis for the 102 clusters in the subsample with  $>2\sigma$  temperature measurements within either 300 kpc or 500 kpc.

ID (eFEDS J+)	ID	SRC	RA	Dec	$L_{\text{ext}}$	$L_{\text{det}}$	$L_{300\text{kpc}}$	$T_{\text{sphere}}$	$L_{400\text{kpc}}$	$L_{500\text{kpc}}$	$L_{\text{bol}, 300\text{kpc}}$	$F_{300\text{kpc}}$	$F_{500\text{kpc}}$	$\text{SN}_{\text{max}}$	$R(\text{SN}_{\text{max}})$	
082808.3-001003	4800	127.03666	-0.16777	28.5	62.5	0.08	0.89 <sub>+0.11</sub> <sup>-0.09</sup>	0.88 <sub>+0.09</sub> <sup>-0.07</sup>	0.26 <sub>+0.04</sub> <sup>-0.03</sup>	0.28 <sub>+0.06</sub> <sup>-0.05</sup>	0.40 <sub>+0.05</sub> <sup>-0.06</sup>	18.02 <sub>+2.64</sub> <sup>-2.58</sup>	19.76 <sub>+4.06</sub> <sup>-4.00</sup>	8.8	2.63	
083204.4-041908	3593	128.01885	+4.3188	66.0	118.6	0.20	2.79 <sub>+0.34</sub> <sup>-0.30</sup>	2.42 <sub>+0.34</sub> <sup>-0.32</sup>	2.08 <sub>+0.22</sub> <sup>-0.21</sup>	3.33 <sub>+0.35</sub> <sup>-0.32</sup>	4.72 <sub>+0.59</sub> <sup>-0.56</sup>	7.59 <sub>+1.89</sub> <sup>-1.84</sup>	31.00 <sub>+3.83</sub> <sup>-3.83</sup>	11.9	3.45	
083304.4-050428	2528	128.3767	+5.0744	50.1	122.2	0.21	2.05 <sub>+0.34</sub> <sup>-0.32</sup>	1.12 <sub>+0.34</sub> <sup>-0.32</sup>	1.54 <sub>+0.21</sub> <sup>-0.20</sup>	3.37 <sub>+0.56</sub> <sup>-0.53</sup>	3.47 <sub>+0.54</sub> <sup>-0.51</sup>	8.69 <sub>+1.54</sub> <sup>-1.50</sup>	11.89 <sub>+2.79</sub> <sup>-2.74</sup>	8.7	2.30	
083651.3-030002	197	129.2138	+3.0006	153.5	747.9	0.192	2.79 <sub>+0.62</sub> <sup>-0.51</sup>	2.57 <sub>+0.51</sub> <sup>-0.43</sup>	3.97 <sub>+0.26</sub> <sup>-0.24</sup>	9.19 <sub>+0.51</sub> <sup>-0.49</sup>	11.43 <sub>+0.68</sub> <sup>-0.66</sup>	39.07 <sub>+1.99</sub> <sup>-1.96</sup>	48.66 <sub>+2.10</sub> <sup>-2.09</sup>	23.1	2.89	
083654.6-025954	16471	129.2277	+2.9984	10.9	14.0	0.191	2.55 <sub>+0.62</sub> <sup>-0.53</sup>	2.65 <sub>+0.57</sub> <sup>-0.48</sup>	3.95 <sub>+0.28</sub> <sup>-0.26</sup>	9.49 <sub>+0.52</sub> <sup>-0.50</sup>	9.28 <sub>+0.73</sub> <sup>-0.71</sup>	39.43 <sub>+1.75</sub> <sup>-1.72</sup>	49.29 <sub>+2.04</sub> <sup>-2.01</sup>	23.1	2.87	
083807.7-002501	19692	129.5321	+0.4171	6.4	15.1	0.080	-	0.48 <sub>+0.35</sub> <sup>-0.35</sup>	0.12 <sub>+0.30</sub> <sup>-0.29</sup>	0.15 <sub>+0.07</sub> <sup>-0.06</sup>	0.19 <sub>+0.07</sub> <sup>-0.06</sup>	0.25 <sub>+0.05</sub> <sup>-0.05</sup>	7.19 <sub>+0.56</sub> <sup>-0.55</sup>	9.36 <sub>+2.57</sub> <sup>-2.57</sup>	6.0	3.38
083812.0-015934	53	129.5496	-1.9930	163.7	2105.1	0.56	4.27 <sub>+1.12</sub> <sup>-1.04</sup>	4.72 <sub>+0.94</sub> <sup>-0.88</sup>	37.04 <sub>+3.37</sub> <sup>-3.37</sup>	39.98 <sub>+3.45</sub> <sup>-3.45</sup>	112.88 <sub>+1.66</sub> <sup>-1.66</sup>	122.00 <sub>+0.57</sub> <sup>-0.57</sup>	34.54 <sub>+2.94</sub> <sup>-2.94</sup>	37.32 <sub>+2.98</sub> <sup>-2.98</sup>	23.4	1.25
083817.4-041822	6136	129.5727	+4.3060	21.1	56.6	0.211	-	1.41 <sub>+0.98</sub> <sup>-0.94</sup>	1.72 <sub>+0.84</sub> <sup>-0.81</sup>	1.05 <sub>+0.24</sub> <sup>-0.23</sup>	1.32 <sub>+0.25</sub> <sup>-0.25</sup>	1.90 <sub>+0.39</sub> <sup>-0.39</sup>	5.51 <sub>+1.03</sub> <sup>-1.03</sup>	7.99 <sub>+1.76</sub> <sup>-1.76</sup>	7.8	2.33
083857.6-020847	1806	129.7398	+2.1464	92.8	192.1	0.360	2.81 <sub>+1.30</sub> <sup>-1.30</sup>	3.01 <sub>+0.78</sub> <sup>-0.77</sup>	4.55 <sub>+0.38</sub> <sup>-0.38</sup>	7.23 <sub>+0.51</sub> <sup>-0.50</sup>	11.30 <sub>+1.55</sub> <sup>-1.55</sup>	18.03 <sub>+2.20</sub> <sup>-2.20</sup>	11.05 <sub>+1.96</sub> <sup>-1.96</sup>	17.64 <sub>+2.02</sub> <sup>-2.02</sup>	14.6	2.74
083900.6-020057	736	129.7527	+2.0159	39.3	313.3	0.359	2.26 <sub>+0.69</sub> <sup>-0.68</sup>	2.28 <sub>+0.62</sub> <sup>-0.62</sup>	5.24 <sub>+0.41</sub> <sup>-0.41</sup>	5.84 <sub>+0.63</sub> <sup>-0.62</sup>	7.05 <sub>+1.08</sub> <sup>-1.08</sup>	11.32 <sub>+1.55</sub> <sup>-1.55</sup>	12.31 <sub>+1.45</sub> <sup>-1.45</sup>	9.09 <sub>+1.18</sub> <sup>-1.18</sup>	12.5	1.26
083933.9-014044	356	129.8809	-1.6790	245.8	663.7	0.272	4.14 <sub>+0.43</sub> <sup>-0.43</sup>	3.74 <sub>+0.49</sub> <sup>-0.49</sup>	7.47 <sub>+0.52</sub> <sup>-0.52</sup>	11.22 <sub>+0.58</sub> <sup>-0.58</sup>	20.31 <sub>+1.58</sub> <sup>-1.58</sup>	30.50 <sub>+1.43</sub> <sup>-1.43</sup>	34.82 <sub>+1.36</sub> <sup>-1.36</sup>	52.53 <sub>+1.38</sub> <sup>-1.38</sup>	24.5	2.98
083940.8-010417	2832	129.9201	+1.0714	27.3	84.0	0.157	1.44 <sub>+0.80</sub> <sup>-0.76</sup>	1.22 <sub>+0.76</sub> <sup>-0.72</sup>	0.61 <sub>+0.07</sub> <sup>-0.07</sup>	0.74 <sub>+0.02</sub> <sup>-0.02</sup>	1.03 <sub>+0.06</sub> <sup>-0.06</sup>	1.26 <sub>+0.19</sub> <sup>-0.19</sup>	1.89 <sub>+0.39</sub> <sup>-0.39</sup>	10.92 <sub>+1.63</sub> <sup>-1.63</sup>	9.1	2.07
084034.6-023639	250	130.1441	+2.6108	114.6	661.8	0.049	0.80 <sub>+0.02</sub> <sup>-0.02</sup>	0.82 <sub>+0.08</sub> <sup>-0.08</sup>	0.11 <sub>+0.01</sub> <sup>-0.01</sup>	0.17 <sub>+0.02</sub> <sup>-0.02</sup>	0.17 <sub>+0.02</sub> <sup>-0.02</sup>	0.17 <sub>+0.02</sub> <sup>-0.02</sup>	18.86 <sub>+1.95</sub> <sup>-1.95</sup>	18.96 <sub>+1.95</sub> <sup>-1.95</sup>	15.2	1.47
084105.5-031640	1906	130.2731	+3.2777	32.3	146.2	0.34	2.72 <sub>+0.72</sub> <sup>-0.72</sup>	-	2.78 <sub>+0.69</sub> <sup>-0.69</sup>	3.56 <sub>+0.69</sub> <sup>-0.69</sup>	6.86 <sub>+0.92</sub> <sup>-0.92</sup>	8.86 <sub>+1.30</sub> <sup>-1.30</sup>	10.14 <sub>+1.68</sub> <sup>-1.68</sup>	9.9	1.66	
084221.0-013844	3295	130.3875	+1.6457	47.7	64.5	0.421	-	2.06 <sub>+0.97</sub> <sup>-0.97</sup>	3.37 <sub>+0.36</sub> <sup>-0.36</sup>	5.65 <sub>+0.36</sub> <sup>-0.36</sup>	7.05 <sub>+1.08</sub> <sup>-1.08</sup>	11.85 <sub>+1.70</sub> <sup>-1.70</sup>	5.42 <sub>+0.92</sub> <sup>-0.92</sup>	9.09 <sub>+1.18</sub> <sup>-1.18</sup>	10.0	2.48
084418.0-010416	1812	13.0748	+1.0711	26.0	94.6	0.340	2.46 <sub>+1.24</sub> <sup>-1.24</sup>	-	3.31 <sub>+0.46</sub> <sup>-0.46</sup>	4.40 <sub>+0.66</sub> <sup>-0.66</sup>	8.44 <sub>+0.92</sub> <sup>-0.92</sup>	11.19 <sub>+1.53</sub> <sup>-1.53</sup>	12.32 <sub>+1.16</sub> <sup>-1.16</sup>	10.2	1.70	
084528.7-032739	144	131.3695	+3.4609	316.7	1183.0	0.334	6.68 <sub>+1.92</sub> <sup>-1.92</sup>	6.31 <sub>+1.93</sub> <sup>-1.93</sup>	12.99 <sub>+0.84</sub> <sup>-0.84</sup>	18.49 <sub>+1.79</sub> <sup>-1.79</sup>	44.96 <sub>+4.55</sub> <sup>-4.55</sup>	64.06 <sub>+5.27</sub> <sup>-5.27</sup>	56.55 <sub>+2.43</sub> <sup>-2.43</sup>	26.1	2.90	
084531.6-022831	1039	131.3818	+2.4753	98.9	275.7	0.076	1.45 <sub>+0.62</sub> <sup>-0.61</sup>	1.27 <sub>+0.61</sub> <sup>-0.61</sup>	0.41 <sub>+0.03</sub> <sup>-0.03</sup>	0.43 <sub>+0.03</sub> <sup>-0.03</sup>	0.72 <sub>+0.05</sub> <sup>-0.05</sup>	0.76 <sub>+0.05</sub> <sup>-0.05</sup>	18.86 <sub>+1.95</sub> <sup>-1.95</sup>	18.96 <sub>+1.95</sub> <sup>-1.95</sup>	14.8	2.63
084544.4-002914	2214	131.4349	-0.4874	33.5	103.1	0.156	1.72 <sub>+0.62</sub> <sup>-0.62</sup>	-	2.78 <sub>+0.69</sub> <sup>-0.69</sup>	3.56 <sub>+0.69</sub> <sup>-0.69</sup>	6.86 <sub>+0.92</sub> <sup>-0.92</sup>	8.86 <sub>+1.30</sub> <sup>-1.30</sup>	10.14 <sub>+1.68</sub> <sup>-1.68</sup>	9.9	1.66	
084645.7-014947	6215	131.6902	+1.8298	12.4	39.2	0.051	0.50 <sub>+0.06</sub> <sup>-0.06</sup>	0.49 <sub>+0.06</sub> <sup>-0.06</sup>	0.09 <sub>+0.01</sub> <sup>-0.01</sup>	0.11 <sub>+0.01</sub> <sup>-0.01</sup>	0.14 <sub>+0.02</sub> <sup>-0.02</sup>	0.17 <sub>+0.03</sub> <sup>-0.03</sup>	14.12 <sub>+1.27</sub> <sup>-1.27</sup>	17.08 <sub>+2.30</sub> <sup>-2.30</sup>	11.5	2.14
085027.9-0101503	1023	132.6160	+0.2509	128.7	280.4	0.197	3.56 <sub>+0.68</sub> <sup>-0.68</sup>	2.99 <sub>+0.63</sub> <sup>-0.63</sup>	2.88 <sub>+0.08</sub> <sup>-0.08</sup>	4.36 <sub>+0.29</sub> <sup>-0.29</sup>	7.06 <sub>+0.62</sub> <sup>-0.62</sup>	10.71 <sub>+0.91</sub> <sup>-0.91</sup>	12.13 <sub>+1.18</sub> <sup>-1.18</sup>	41.04 <sub>+3.23</sub> <sup>-3.23</sup>	18.6	4.19
085120.0-022952	2101	132.8333	+2.4977	54.7	133.3	0.38	-	2.33 <sub>+0.78</sub> <sup>-0.78</sup>	1.23 <sub>+0.65</sub> <sup>-0.65</sup>	5.90 <sub>+0.74</sub> <sup>-0.74</sup>	8.43 <sub>+0.85</sub> <sup>-0.85</sup>	12.81 <sub>+1.52</sub> <sup>-1.52</sup>	12.09 <sub>+1.63</sub> <sup>-1.63</sup>	17.28 <sub>+2.48</sub> <sup>-2.48</sup>	9.7	1.94
085419.6-000925	1294	133.5814	-0.1572	56.0	110.0	0.282	1.97 <sub>+0.78</sub> <sup>-0.78</sup>	-	2.64 <sub>+0.74</sub> <sup>-0.74</sup>	3.75 <sub>+0.74</sub> <sup>-0.74</sup>	5.99 <sub>+0.84</sub> <sup>-0.84</sup>	6.46 <sub>+0.95</sub> <sup>-0.95</sup>	15.63 <sub>+1.27</sub> <sup>-1.27</sup>	12.9	2.76	
085436.6-003835	328	133.6526	+0.6431	242.8	688.6	0.106	3.39 <sub>+0.90</sub> <sup>-0.90</sup>	2.42 <sub>+0.66</sub> <sup>-0.66</sup>	1.50 <sub>+0.21</sub> <sup>-0.21</sup>	1.83 <sub>+0.24</sub> <sup>-0.24</sup>	3.55 <sub>+0.88</sub> <sup>-0.88</sup>	8.46 <sub>+1.38</sub> <sup>-1.38</sup>	28.55 <sub>+2.46</sub> <sup>-2.46</sup>	14.8	2.63	
085447.1-012132	3128	134.2749	+1.2482	53.7	153.9	0.353	1.79 <sub>+0.35</sub> <sup>-0.35</sup>	1.71 <sub>+0.35</sub> <sup>-0.35</sup>	1.39 <sub>+0.31</sub> <sup>-0.31</sup>	1.39 <sub>+0.31</sub> <sup>-0.31</sup>	4.64 <sub>+0.84</sub> <sup>-0.84</sup>	9.81 <sub>+1.41</sub> <sup>-1.41</sup>	17.92 <sub>+2.92</sub> <sup>-2.92</sup>	21.17 <sub>+3.39</sub> <sup>-3.39</sup>	11.5	2.14
085706.0-011453	2079	133.6962	-1.3591	81.5	153.9	0.106	1.10 <sub>+0.36</sub> <sup>-0.36</sup>	0.87 <sub>+0.73</sub> <sup>-0.73</sup>	0.87 <sub>+0.73</sub> <sup>-0.73</sup>	0.51 <sub>+0.08</sub> <sup>-0.08</sup>	0.70 <sub>+0.08</sub> <sup>-0.08</sup>	0.79 <sub>+0.08</sub> <sup>-0.08</sup>	15.31 <sub>+1.44</sub> <sup>-1.44</sup>	17.33 <sub>+2.39</sub> <sup>-2.39</sup>	11.5	2.14
085751.7-0131039	108	134.4653	+1.1775	742.2	2053.9	0.201	5.79 <sub>+0.19</sub> <sup>-0.19</sup>	5.65 <sub>+0.19</sub> <sup>-0.19</sup>	5.95 <sub>+0.04</sub> <sup>-0.04</sup>	9.59 <sub>+0.04</sub> <sup>-0.04</sup>	13.54 <sub>+0.56</sub> <sup>-0.56</sup>	44.44 <sub>+1.07</sub> <sup>-1.07</sup>	9.05 <sub>+0.97</sub> <sup>-0.97</sup>	9.3	2.54	
085804.9-013508	6746	133.8219	+1.5875	36.4	90.8	0.071	1.29 <sub>+0.26</sub> <sup>-0.26</sup>	1.12 <sub>+0.18</sub> <sup>-0.18</sup>	0.24 <sub>+0.05</sub> <sup>-0.05</sup>	0.29 <sub>+0.05</sub> <sup>-0.05</sup>	0.40 <sub>+0.07</sub> <sup>-0.07</sup>	6.94 <sub>+0.95</sub> <sup>-0.95</sup>	9.51 <sub>+1.74</sub> <sup>-1.74</sup>	23.42 <sub>+4.88</sub> <sup>-4.88</sup>	11.5	2.93
085849.8-022800	715	134.7076	+2.4668	25.8	304.5	0.168	1.81 <sub>+0.38</sub> <sup>-0.38</sup>	1.82 <sub>+0.34</sub> <sup>-0.34</sup>	1.81 <sub>+0.14</sub> <sup>-0.14</sup>	2.14 <sub>+0.05</sub> <sup>-0.05</sup>	2.71 <sub>+0.07</sub> <sup>-0.07</sup>	4.39 <sub>+0.84</sub> <sup>-0.84</sup>	5.55 <sub>+1.07</sub> <sup>-1.07</sup>	15.97 <sub>+2.98</sub> <sup>-2.98</sup>	14.4	2.35
085901.6-010649	2757	134.7564	+1.1137	33.6	97.4	0.162	-	0.97 <sub>+0.76</sub> <sup>-0.76</sup>	0.56 <sub>+0.68</sub> <sup>-0.68</sup>	0.61 <sub>+0.08</sub> <sup>-0.08</sup>	0.58 <sub>+0.08</sub> <sup>-0.08</sup>	0.58 <sub>+0.08</sub> <sup>-0.08</sup>	0.76 <sub>+1.33</sub> <sup>-1.33</sup>	8.22 <sub>+2.67</sub> <sup>-2.67</sup>	8.4	1.53
085913.1-031335	485	134.8048	+3.2263	15.9	16.8	0.189	1.27 <sub>+0.35</sub> <sup>-0.35</sup>	1.11 <sub>+0.26</sub> <sup>-0.26</sup>	1.14 <sub>+0.08</sub> <sup>-0.08</sup>	1.26 <sub>+0.08</sub> <sup>-0.08</sup>	1.84 <sub>+0.24</sub> <sup>-0.24</sup>	2.04 <sub>+0.36</sub> <sup>-0.36</sup>	10.87 <sub>+1.43</sub> <sup>-1.43</sup>	15.31 <sub>+1.44</sub> <sup>-1.44</sup>	11.7	2.51
085931.9-030839	360	134.8830	+3.1443	175.1	617.4	0.201	2.62 <sub>+0.35</sub> <sup>-0.35</sup>	2.37 <sub>+0.30</sub> <sup>-0.30</sup>	1.27 <sub>+0.17</sub> <sup>-0.17</sup>	1.27 <sub>+0.17</sub> <sup>-0.17</sup>	2.72 <sub>+0.23</sub> <sup>-0.23</sup>	7.27 <sub>+0.73</sub> <sup>-0.73</sup>	12.07 <sub>+2.57</sub> <sup>-2.57</sup>	38.61 <sub>+2.53</sub> <sup>-2.53</sup>	20.2	4.37
085949.9-041120	1350	134.9539	+4.1889	22.6	43.0	0.208	1.63 <sub>+0.36</sub> <sup>-0.36</sup>	1.37 <sub>+0.34</sub> <sup>-0.34</sup>	1.25 <sub>+0.13</sub> <sup>-0.13</sup>	1.25 <sub>+0.13</sub> <sup>-0.13</sup>	2.25 <sub>+0.38</sub> <sup>-0.38</sup>	2.63 <sub>+0.56</sub> <sup>-0.56</sup>	9.93 <sub>+1.69</sub> <sup>-1.69</sup>	11.60 <sub>+1.71</sub> <sup>-1.71</sup>	10.7	1.66
090104.5-011643	3171	135.2686	+1.2788	38.0	62.8	0.251	-	1.61 <sub>+0.20</sub> <sup>-0.20</sup>	1.61 <sub>+0.18</sub> <sup>-0.18</sup>	1.65 <sub>+0.02</sub> <sup>-0.02</sup>	2.03 <sub>+0.15</sub> <sup>-0.15</sup>	3.21 <sub>+0.28</sub> <sup>-0.28</sup>	3.94 <sub>+0.84</sub> <sup>-0.84</sup>	8.71 <sub>+1.04</sub> <sup>-1.04</sup>	10.76 <sub>+1.24</sub> <sup>-1</sup>	

Table B.2. continued.

ID (eFEDS J+)	ID_SRC	RA	Dec	$\mathcal{L}_{\text{ext}}$	$\mathcal{L}_{\text{det}}$	$z$	$T_{300\text{kpc}}$	$T_{500\text{kpc}}$	$L_{300\text{kpc}}$	$L_{500\text{kpc}}$	$L_{\text{bol},300\text{kpc}}$	$L_{\text{bol},500\text{kpc}}$	$F_{300\text{kpc}}$	$F_{500\text{kpc}}$	$R(\text{SN}_{\text{max}})$	
091417.7-031159	396	138.5740	+3.1998	16.7	26.9	0.231	0.96 $^{+0.34}$	1.12 $^{+0.38}$	1.15 $^{+0.33}$	1.78 $^{+0.52}$	1.81 $^{+0.43}$	6.78 $^{+1.77}$	6.96 $^{+1.99}$	13.3	0.70	
091453.6-041613	372	138.7235	+4.2704	123.9	398.6	0.143	2.81 $^{+0.37}$	2.15 $^{+0.34}$	2.23 $^{+0.35}$	2.66 $^{+0.37}$	5.83 $^{+0.47}$	4.91 $^{+0.62}$	22.7	2.91		
091509.5-051521	6244	138.7937	+5.2560	48.0	70.0	0.25	1.83 $^{+0.35}$	2.37 $^{+0.31}$	3.96 $^{+0.34}$	4.90 $^{+0.41}$	12.89 $^{+1.30}$	21.41 $^{+2.49}$	10.7	3.19		
091610.2-002348	534	139.0423	-0.3969	282.2	623.3	0.322	3.83 $^{+0.77}$	4.45 $^{+0.38}$	8.66 $^{+0.32}$	15.51 $^{+0.44}$	25.51 $^{+0.33}$	45.50 $^{+0.97}$	28.22 $^{+1.48}$	50.53 $^{+2.61}$	27.1	3.04
091722.5-010118	1526	139.3435	+1.0218	56.4	187.8	0.359	-	2.61 $^{+0.36}$	3.68 $^{+0.44}$	4.67 $^{+0.32}$	8.44 $^{+1.02}$	10.67 $^{+1.08}$	8.85 $^{+1.02}$	11.21 $^{+1.08}$	10.9	1.60
091849.0-021205	994	139.7042	+2.2013	94.8	245.3	0.283	3.64 $^{+1.69}$	3.63 $^{+0.62}$	3.68 $^{+0.34}$	9.78 $^{+1.30}$	15.56 $^{+0.37}$	15.74 $^{+0.95}$	25.17 $^{+1.84}$	17.8	3.06	
091858.0-024946	7194	139.7418	+2.8295	26.3	46.3	0.199	1.28 $^{+0.30}$	0.76 $^{+0.30}$	0.70 $^{+0.32}$	1.31 $^{+0.38}$	1.79 $^{+0.26}$	6.58 $^{+0.33}$	8.97 $^{+1.08}$	8.1	2.08	
092037.2-013444	222	140.0545	+1.5789	88.4	719.6	0.71	2.26 $^{+0.58}$	2.44 $^{+0.50}$	25.58 $^{+0.90}$	30.67 $^{+1.28}$	55.97 $^{+1.35}$	66.88 $^{+1.95}$	11.97 $^{+1.81}$	14.20 $^{+2.36}$	16.5	1.39
092037.1-011506	5739	140.1545	-1.2519	34.3	63.0	0.154	1.01 $^{+0.13}$	1.16 $^{+0.35}$	0.48 $^{+0.45}$	0.61 $^{+0.38}$	0.81 $^{+0.35}$	1.03 $^{+0.35}$	7.40 $^{+1.68}$	9.39 $^{+1.26}$	8.6	2.15
092046.3-002849	1915	140.1926	+0.4803	40.0	69.6	0.413	-	1.97 $^{+0.22}$	3.71 $^{+0.38}$	5.56 $^{+0.38}$	7.70 $^{+0.08}$	11.54 $^{+0.52}$	6.21 $^{+0.88}$	9.31 $^{+0.88}$	11.4	2.64
092049.5-024513	489	140.2063	+2.7538	142.1	514.2	0.284	2.88 $^{+0.72}$	3.39 $^{+0.89}$	5.63 $^{+0.34}$	8.39 $^{+0.30}$	14.65 $^{+0.37}$	21.77 $^{+1.96}$	35.62 $^{+1.61}$	23.0	3.08	
092121.2-031726	100	140.3385	+3.2906	478.6	1729.7	0.333	4.81 $^{+0.83}$	5.25 $^{+0.94}$	15.28 $^{+0.78}$	21.43 $^{+0.76}$	47.50 $^{+0.96}$	66.88 $^{+1.24}$	46.65 $^{+1.24}$	65.20 $^{+2.88}$	31.6	2.80
092202.3-034520	5347	140.5095	+3.7557	43.4	66.6	0.319	5.42 $^{+0.67}$	5.28 $^{+0.63}$	4.22 $^{+0.63}$	7.72 $^{+0.72}$	13.28 $^{+1.28}$	13.28 $^{+1.28}$	8.31 $^{+0.95}$	14.20 $^{+2.45}$	13.2	2.60
092209.4-034628	367	140.5391	+3.7746	369.9	783.1	0.270	4.25 $^{+1.25}$	5.39 $^{+1.38}$	5.76 $^{+0.34}$	18.11 $^{+2.38}$	24.93 $^{+1.98}$	28.01 $^{+0.45}$	38.73 $^{+5.01}$	23.1	2.80	
092220.4-034806	4014	140.5852	+3.8017	24.1	48.9	0.267	-	2.31 $^{+0.32}$	1.24 $^{+0.32}$	1.53 $^{+0.31}$	2.87 $^{+0.62}$	3.52 $^{+0.98}$	5.90 $^{+0.94}$	7.27 $^{+1.82}$	8.5	1.48
092235.9-002443	3133	140.6494	-0.4120	30.2	49.4	0.055	1.90 $^{+0.59}$	2.23 $^{+0.52}$	0.15 $^{+0.03}$	0.16 $^{+0.08}$	0.33 $^{+0.03}$	0.34 $^{+0.07}$	20.84 $^{+0.86}$	21.67 $^{+0.75}$	11.9	2.16
092242.0-020720	1535	140.6749	+2.1222	32.5	52.2	0.198	-	1.29 $^{+0.37}$	0.79 $^{+0.34}$	0.93 $^{+0.34}$	1.37 $^{+0.35}$	1.61 $^{+0.27}$	6.91 $^{+1.19}$	8.15 $^{+1.38}$	8.6	1.60
092339.0-052655	1894	140.9129	+5.4486	30.3	158.3	0.37	2.52 $^{+0.58}$	3.93 $^{+0.46}$	35.48 $^{+0.75}$	36.83 $^{+1.30}$	98.68 $^{+1.50}$	101.13 $^{+2.04}$	81.89 $^{+2.09}$	84.78 $^{+2.09}$	16.3	1.02
092405.1-013059	298	141.0231	-1.5165	66.6	576.5	0.337	-	3.71 $^{+0.34}$	5.76 $^{+0.34}$	7.98 $^{+1.08}$	10.24 $^{+0.89}$	13.25 $^{+1.30}$	10.80 $^{+1.36}$	14.06 $^{+1.49}$	16.7	1.84
092409.4-040057	1437	141.0393	+4.0160	122.1	238.5	0.084	-	0.92 $^{+0.08}$	0.36 $^{+0.03}$	0.40 $^{+0.03}$	0.56 $^{+0.04}$	0.63 $^{+0.05}$	22.72 $^{+1.23}$	14.8	2.81	
092533.7-014205	1483	141.3903	-1.7016	51.0	150.6	0.23	-	2.30 $^{+0.32}$	1.03 $^{+0.32}$	1.22 $^{+0.32}$	2.29 $^{+0.32}$	2.71 $^{+0.95}$	6.82 $^{+1.43}$	8.01 $^{+0.95}$	11.2	1.54
092546.4-014347	566	141.4432	-1.7298	197.1	480.2	0.23	-	2.64 $^{+0.44}$	2.23 $^{+0.40}$	2.98 $^{+0.33}$	5.21 $^{+0.65}$	6.96 $^{+0.89}$	15.01 $^{+0.95}$	20.04 $^{+0.95}$	18.3	2.24
092629.4-032614	2050	141.6225	+3.4374	19.7	117.5	0.088	0.90 $^{+0.07}$	0.94 $^{+0.05}$	0.24 $^{+0.20}$	0.30 $^{+0.05}$	0.38 $^{+0.05}$	0.47 $^{+0.08}$	12.24 $^{+1.36}$	15.24 $^{+1.64}$	9.3	2.49
092647.5-050033	137	141.6980	+5.0091	505.4	1395.7	0.337	-	6.72 $^{+0.87}$	18.64 $^{+1.58}$	25.68 $^{+0.93}$	65.64 $^{+1.26}$	90.24 $^{+1.35}$	10.46 $^{+1.36}$	10.46 $^{+1.36}$	23.6	2.28
092648.0-050124	6875	141.7002	+5.0024	16.0	26.5	0.45	7.04 $^{+4.00}$	5.77 $^{+1.78}$	9.45 $^{+2.13}$	21.70 $^{+8.39}$	31.16 $^{+1.86}$	10.47 $^{+4.05}$	13.3	1.84		
092650.5-035755	671	141.7106	+3.9654	33.0	304.8	0.377	2.86 $^{+0.38}$	2.59 $^{+0.38}$	4.59 $^{+0.38}$	4.97 $^{+0.61}$	10.53 $^{+1.88}$	11.29 $^{+1.62}$	10.56 $^{+1.33}$	11.3	1.06	
092735.4-014423	266	141.8974	+1.7399	32.9	43.2	0.149	-	1.90 $^{+0.45}$	0.82 $^{+0.32}$	0.98 $^{+0.32}$	1.74 $^{+0.42}$	2.06 $^{+0.61}$	12.03 $^{+0.70}$	16.62 $^{+2.76}$	12.1	2.15
092737.8-020607	1924	141.9074	+2.1021	106.4	191.5	0.419	-	2.82 $^{+0.45}$	0.94 $^{+0.45}$	0.24 $^{+0.20}$	0.30 $^{+0.05}$	0.38 $^{+0.05}$	18.04 $^{+1.97}$	18.15 $^{+1.97}$	11.8	2.04
092821.2-042149	666	142.0884	+4.3637	113.0	375.3	0.23	3.41 $^{+0.88}$	1.44 $^{+0.44}$	2.29 $^{+0.36}$	4.08 $^{+0.89}$	4.08 $^{+0.89}$	9.09 $^{+0.97}$	10.24 $^{+1.26}$	15.7	2.22	
092915.8-001357	1549	142.3237	-0.3237	31.5	181.0	0.322	1.83 $^{+0.49}$	1.04 $^{+0.44}$	2.66 $^{+0.54}$	4.19 $^{+0.87}$	4.65 $^{+0.87}$	5.06 $^{+0.89}$	6.62 $^{+0.92}$	8.01 $^{+1.04}$	9.4	1.36
092921.8-040040	609	142.3408	+4.0112	51.8	297.4	0.50	3.39 $^{+0.33}$	1.39 $^{+0.34}$	9.37 $^{+0.30}$	22.82 $^{+0.59}$	25.63 $^{+0.75}$	9.77 $^{+0.76}$	10.91 $^{+0.52}$	11.6	1.12	
092955.9-003403	1967	142.4829	-0.5676	39.4	137.1	0.150	1.76 $^{+0.28}$	1.67 $^{+0.41}$	0.92 $^{+0.35}$	1.43 $^{+0.40}$	1.78 $^{+0.37}$	12.14 $^{+1.20}$	15.19 $^{+1.34}$	11.1	2.35	
093033.3-035630	288	142.5140	+3.9417	82.1	593.1	0.327	2.22 $^{+0.62}$	2.81 $^{+0.72}$	6.01 $^{+0.53}$	6.48 $^{+0.38}$	14.40 $^{+0.67}$	15.51 $^{+1.64}$	18.08 $^{+1.68}$	19.53 $^{+1.88}$	15.3	1.30
093009.0-040144	536	142.5376	+4.0289	76.4	376.0	0.328	2.59 $^{+0.34}$	2.05 $^{+0.34}$	5.04 $^{+0.34}$	10.65 $^{+1.38}$	11.66 $^{+1.56}$	13.68 $^{+1.56}$	14.93 $^{+1.56}$	13.0	1.30	
093141.3-004717	1705	142.9219	-0.7883	13.7	30.9	0.093	-	0.50 $^{+0.09}$	0.13 $^{+0.04}$	0.21 $^{+0.04}$	0.21 $^{+0.06}$	0.21 $^{+0.06}$	6.21 $^{+0.71}$	7.8	1.52	
093149.9-020144	6494	142.9576	-0.2089	27.5	39.9	0.13	1.01 $^{+0.09}$	0.97 $^{+0.10}$	0.18 $^{+0.04}$	0.23 $^{+0.04}$	0.29 $^{+0.06}$	0.37 $^{+0.07}$	3.77 $^{+0.38}$	14.2	2.16	
093151.3-002212	836	142.9638	-0.3701	54.0	307.1	0.336	2.53 $^{+0.38}$	2.36 $^{+0.38}$	4.00 $^{+0.38}$	4.77 $^{+0.48}$	8.74 $^{+0.48}$	10.46 $^{+0.71}$	11.08 $^{+0.72}$	12.1	1.52	
093403.6-001422	900	143.5148	-0.2397	79.7	279.5	0.24	1.87 $^{+0.37}$	1.78 $^{+0.24}$	2.43 $^{+0.38}$	3.02 $^{+0.38}$	4.92 $^{+0.59}$	6.07 $^{+0.83}$	14.30 $^{+1.76}$	17.71 $^{+1.66}$	13.6	2.04
093431.3-002309	1641	143.6304	-0.3860	35.5	87.4	0.342	3.02 $^{+0.26}$	3.06 $^{+0.26}$	4.85 $^{+0.36}$	12.42 $^{+1.26}$	17.91 $^{+2.57}$	9.86 $^{+1.26}$	14.26 $^{+1.42}$	11.8	2.18	
093500.8-005417	649	143.7532	+0.7048	104.4	330.3	0.361	3.27 $^{+0.73}$	2.75 $^{+0.91}$	6.69 $^{+0.32}$	15.07 $^{+2.39}$	18.16 $^{+1.33}$	18.36 $^{+1.35}$	18.36 $^{+1.35}$	14.2	2.16	
093513.1-004757	213	143.8046	+0.7994	332.8	836.9	0.356	5.32 $^{+0.54}$	6.29 $^{+0.57}$	12.93 $^{+0.57}$	20.24 $^{+0.72}$	67.25 $^{+1.58}$	33.92 $^{+1.33}$	52.93 $^{+1.33}$	27.5	3.04	
093521.0-023234	82	143.8374	+2.5429	175.9	1645.8	0.516	3.39 $^{+0.89}$	4.38 $^{+1.37}$	2.36 $^{+0.38}$							